Journal of Colloid and Interface Science 662 (2024) 446–459

Contents lists available at ScienceDirect

Journal of Colloid And Interface Science

journal homepage: www.elsevier.com/locate/jcis

Regular Article

Small-angle X-ray scattering unveils the internal structure of lipid nanoparticles

Francesco Spinozzi [a,*], Paolo Moretti [a], Diego Romano Perinelli [b], Giacomo Corucci [c,d,e], Paolo Piergiovanni [a], Heinz Amenitsch [f], Giulio Alfredo Sancini [g], Giancarlo Franzese [h], Paolo Blasi [i,*]

[a] Department of Life and Environmental Sciences, Polytechnic University of Marche, Italy
[b] School of Pharmacy, University of Camerino, Camerino, Italy
[c] Institut Laue-Langevin, Grenoble, France
[d] École Doctorale de Physique, Université Grenoble Alpes, Saint-Martin-d'Héres, France
[e] Department of Chemistry, Imperial College London, London, UK
[f] Institute for Inorganic Chemistry, Graz University of Technology, Graz, Austria
[g] School of Medicine and Surgery, University of Milan Bicocca, Milan, Italy
[h] Secció de Física Estadística i Interdisciplinària, Departament de Física de la Matèria Condensada, & Institut de Nanociència i Nanotecnologia, Universitat de Barcelona, Martí i Franquès 1, Barcelona, 08028, Spain
[i] Department of Pharmacy and Biotechnology, University of Bologna, Bologna, Italy

GRAPHICAL ABSTRACT

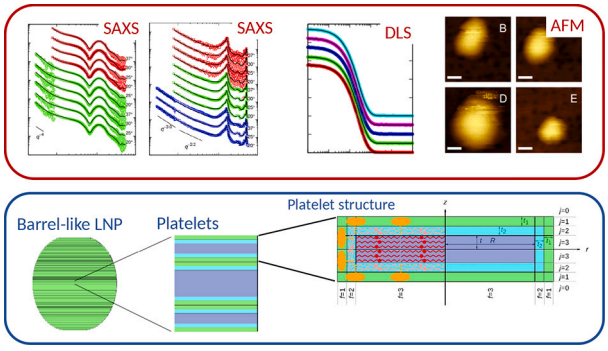

ARTICLE INFO

Keywords:
Core-shell model
Barrel-like structure
Cetyl palmitate
Polysorbate 80 micelles
Critical micellar concentration
Bound water

ABSTRACT

Lipid nanoparticles own a remarkable potential in nanomedicine, only partially disclosed. While the clinical use of liposomes and cationic lipid-nucleic acid complexes is well-established, liquid lipid nanoparticles (nanoemulsions), solid lipid nanoparticles, and nanostructured lipid carriers have even greater possibilities. However, they face obstacles in being used in clinics due to a lack of understanding about the molecular mechanisms controlling their drug loading and release, interactions with the biological environment (such as the protein corona), and shelf-life stability. To create effective drug delivery carriers and successfully translate bench research to clinical settings, it is crucial to have a thorough understanding of the internal structure of lipid nanoparticles. Through synchrotron small-angle X-ray scattering experiments, we determined the spatial distribution and internal structure of the nanoparticles' lipid, surfactant, and the bound water in them. The

* Corresponding authors.
E-mail addresses: f.spinozzi@univpm.it (F. Spinozzi), p.blasi@unibo.it (P. Blasi).

https://doi.org/10.1016/j.jcis.2024.02.076
Received 19 September 2023; Received in revised form 1 February 2024; Accepted 6 February 2024
Available online 12 February 2024
0021-9797/© 2024 The Author(s). Published by Elsevier Inc. This is an open access article under the CC BY-NC-ND license (http://creativecommons.org/licenses/by-nc-nd/4.0/).

nanoparticles themselves have a barrel-like shape that consists of coplanar lipid platelets (specifically cetyl palmitate) that are covered by loosely spaced polysorbate 80 surfactant molecules, whose polar heads retain a large amount of bound water. To reduce the interface cost of bound water with unbound water without stacking, the platelets collapse onto each other. This internal structure challenges the classical core-shell model typically used to describe solid lipid nanoparticles and could play a significant role in drug loading and release, biological fluid interaction, and nanoparticle stability, making our findings valuable for the rational design of lipid-based nanoparticles.

1. Introduction

Lipid nanoparticles (LNPs) have been widely investigated as drug delivery systems for enhancing drug bioavailability and targeting therapeutic and diagnostic agents to pathological sites such as brain and solid tumors [1–6]. The recent introduction to clinics of RNAi and mRNA-based medicinal products using LNPs [7,8] has highlighted the enormous potential of lipid carriers as drug delivery systems for both large biomacromolecules like nucleic acid and peptides, as well as small molecule drugs. However, LNPs comprise a diverse range of nanometer carriers composed of lipid molecules. Indeed, due to the broad definition of lipids according to IUPAC [9], LNPs encompass various structurally different nanoscale carriers, including liposomes, liquid LNPs, solid LNPs, nanostructured lipid carriers, and cationic lipid-nucleic acid complexes [4].

LNPs for drug delivery have the advantage of using GRAS materials [10] and industrial-scale production protocols [4], which increases the likelihood of developing effective nanotechnology-based medicine for clinical use. However, the lack of a deep and comprehensive understanding of the LNP structure hinders the rational, safe and effective design of these drug carriers. The effectiveness and safety of LNPs are not only influenced by the lipids in their formulation and the amount of drug they can hold but also by various factors such as their size, shape, surface chemistry, internal structure, and drug distribution. Careful analysis of the entire system is essential in comprehending the nano-bio interface, which is accountable for the safety and efficacy of nanotechnology-based medication. [11].

Solid LNPs are a type of drug delivery and targeting carriers that have shown great promise due to their stability over time. Compared to other lipid-based delivery systems like liposomes and nanoemulsions, solid LNPs have the solid-state stability of the core that is less prone to problems such as drug leakage/degradation and particle coalescence. They can encapsulate a variety of hydrophobic and hydrophilic drugs [12,13] and this adaptability to deliver a wide range of therapeutic compounds is expected to increase demand for them in the market [14].

Although solid LNPs have shown excellent performance in preclinical studies, they have been studied as nanoscopic carriers for drug delivery and targeting for only the last three decades, much less than liposomes and cationic lipid particles for RNA delivery. Also, solid LNPs still face stability challenges like premature drug leakage and nanoparticle aggregation, which hinder their clinical use [4]. Researchers previously thought lipid polymorphism was responsible for these issues, as observed through techniques like calorimetry and X-ray diffraction. Solid LNPs were described using a core-shell model with a (solid) lipid core stabilized by a surfactant shell, possibly penetrating with its hydrophobic tail the lipid surface [15]. However, recent findings have shown that the interplay between lipids and surfactants is more complex and LNP structure cannot be explained by this model alone [16,17]. This new understanding sheds light on the structure, shelf-life stability, drug loading/release, and interaction with the biological environment of solid LNPs, offering new possibilities for drug delivery.

In this study, we used solid LNPs made of cetyl palmitate (CP) and polysorbate 80 (P80) to investigate how the combination of lipids and surfactants affects the internal lamellar structure and the P80 surface coverage. CP was selected due to its easy biodegradability in vivo [18, 10], fundamental to avoiding waste disposable, while P80 is non-ionic surfactant approved by regulatory agencies for parenteral use and so already employed in injectable formulations [19].

Understanding the internal structure and composition is crucial for predicting drug loading, cargo stability, and release based on the drug's physicochemical properties. Similarly, studying the surface characteristics is essential for analyzing the nano-bio interface and comprehending the role of adsorbed biomolecules (bio-corona) on biodistribution and cellular uptake.

We conducted synchrotron small-angle X-ray scattering (SAXS) experiments on P80 micelles and P80-stabilized LNPs at different concentrations and temperatures. By using advanced methods, we were able to determine that these particles have a barrel-like shape made up of CP platelets that are covered by loosely spaced P80 molecules retaining a large amount of bound water. These findings demonstrate the interplay between lipid, surfactant, and water in the formation of the solid LNP inner core. Furthermore, ≈ 65% of the platelet surface is made of water bound to P80 and in contact with amorphous CP. Consequently, we found that some lipid regions are in contact with the surrounding water via bound water.

2. Materials and methods

2.1. Materials

CP (batch 120851, purity ∼ 93%) was kindly gifted by Gattefossé s.a.s. (Saint-Priest, France) while P80 (batch BCBV8843) was from Sigma-Aldrich (Milan, Italy). Water (resistivity 18.3 MΩcm at 25 °C) was produced with a Synergy® UV Water Purification System (Millipore Sigma, USA). If not specified, all the materials and solvents used in the present research work were used as provided by the supplier without further purification.

2.1.1. Solid LNPs preparation

Solid LNPs were prepared through the hot, high-pressure homogenization technique with slight adaptations of a previously reported protocol [20,21]. Briefly, 4 g of CP, melted at 65 °C, were slowly added to 40 mL of heated water (65 °C) containing P80 at a concentration of 2% (w/v) under mixing at 8000 rpm by a high-shear mixer (Ultra Turrax T25 IKA® Werke GmbH & Co. KG, Staufen, Germany). The obtained emulsion was passed through a homogenizer (high-pressure homogenizer Emulsiflex C5, Avestin Inc., Ottawa, Canada) 7 times at a pressure of 1500 bar [20]. The homogenizer was conditioned at 65 °C during all the homogenization process. After the last homogenization cycle, the obtained nanoemulsion was cooled down in an ice bath, maintaining the dispersion under mild magnetic stirring (20 min). Upon cooling, the nanoemulsion droplets solidify, generating solid LNPs.

2.2. Methods

2.2.1. DLS experiments

Dynamic Light Scattering (DLS) experiments were carried out to evaluate the average size, at micrometric resolution, of solid LNPs as well as their stability as a function of the time from preparation. Measurements were performed on a Zetasizer PRO instrument (Malvern Panalytical Ltd, Malvern, United Kingdom) at 25 °C by detecting the

intensity of the light (wavelength 6328 Å) scattered at a fixed angle of 173°. A freshly prepared dispersion of solid LNPs was diluted to 1 g/L, and three independent DLS measurements of the second-order intensity autocorrelation functions, $g_2(\tau)-1$, where τ is the correlation time, were performed after 0, 2, 6, 15, and 30 days passed from the nanoemulsion preparation. Data were analyzed by assuming a Gaussian distribution of the hydrodynamic LNP radius, R_H, as detailed in the Sect. S1 of the Supplementary Material (SM). Zeta Potential measurements were also performed using the same instrument.

2.2.2. AFM experiments

AFM measurements were carried out on an AIST-NT Scanning Probe Microscopy (Horiba Scientific, Kyoto, Japan). Images were generated in non-contact mode with a pyramidal silicon tip with radius 80 Å. To improve the quality of the measurements, samples were diluted to 0.1 g/L. An amount of ≈ 5 µL of the diluted dispersion was deposited on a freshly cleaved mica surface and then dried with a nitrogen flux. All images were acquired with a resolution of 512 × 512 pixels at a scan rate of 1 Hz and were analyzed with Gwyddion [22] and ImageJ [23] software. The AFM particle size analysis was carried out by selecting about 50 individual LNPs and measuring the distance R_c between the center and the border along randomly oriented straight lines passing through the center of the particle. A histogram of all measurements was then determined by using a 50 Å grid and fitted using a simple Gaussian distribution.

2.2.3. SAXS experiments

SAXS experiments were carried out at the beamline ID02 of ESRF, the European Synchrotron Radiation Facility (Grenoble, France). A unique flow-through capillary, with quartz walls of 10 µm and a diameter of ∼ 2.0 mm, equipped with a motorized syringe that allowed the sample volume to be moved continuously forward and backward in order to limit the radiation damage, was used for both samples and buffers. Two sample-to-detector distances were used, corresponding to 1.5 m and 15 m, and data were merged to achieve a q-range ($q = 4\pi \sin\theta/\lambda$ being the modulus of the scattering vector, where 2θ is the scattering angle and $\lambda = 0.995$ Å the X-ray wavelength) of $0.001 - 0.5$ Å^{-1}. For each of the two distances, SAXS measurements were performed at the temperature of 20, 25, 30, 37, 25 and 20 °C by using an increasing and decreasing temperature ramp accessible using a Peltier-controlled stage. 2D SAXS patterns were collected by using a CCD detector (Rayonix MX170 HS) and subsequently corrected for the CCD dark counts, for the spatial inhomogeneities of the detector and normalized to an absolute scale using the standard procedure [24]. Ten 2D SAXS patterns of 0.1 s duration were collected for each sample or buffer. The 1D SAXS profiles were obtained by azimuthally averaging each of the 10 normalized 2D SAXS patterns. The mean and the standard deviation of the 1D SAXS profiles were calculated based on the 10 2D SAXS patterns. To each sample, the buffer contribution, multiplied by the factor $1-\eta$, η being the sample volume fraction, was subtracted from the 1D SAXS profile to finally obtain the macroscopic differential scattering cross-section, $d\Sigma/d\Omega(q)$, together with its standard deviation, $\sigma(q)$, as a function of q.

Other SAXS experiments on a second batch of samples prepared with the same method exposed in the Sect. 2.1.1 were performed at the Austrian SAXS beamline of the ELETTRA synchrotron (Trieste, Italy). Measurements of both samples and buffers were carried out in a unique quartz capillary (diameter 1.5 mm and wall thickness 10 µm) mounted on a thermostatic support connected to a circulation bath for temperature control. 2D SAXS patterns were collected 3 times with an acquisition time of 20 s using a Pilatus3 1 M detector. Data reduction was performed with the methodology previously described for the ESRF data.

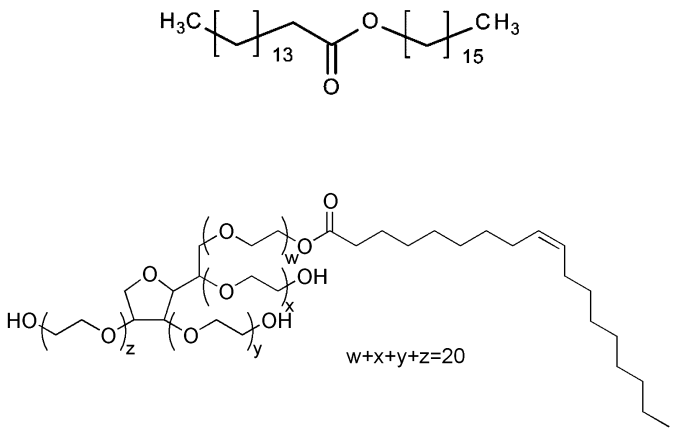

Fig. 1. Chemical structure of the molecules cetyl palmitate, CP (top), and polysorbate 80, P80 (bottom).

2.2.4. SAXS models

We have developed novel models to analyze SAXS data of solid lipid nanoparticles formed by cetyl palmitate and stabilized by polysorbate 80 (Fig. 1) as well as SAXS data of only P80. The models take into account the whole q-range of all synchrotron SAXS data and exploit the information coming from (i) the absolute calibration of such data, (ii) the chemical compositions of CP and P80 (Table 1) and (iii) their nominal concentrations in the SAXS investigated water solutions. Moreover, those models are applied to simultaneously fit all the experimental SAXS curves by following a so-called global fit approach [25].

Data of samples containing only P80 have been analyzed with the form factor of cylinders with spherical end-caps [26], with size distribution described by the ladder model [27], and with the structure factor derived by a perturbation of the Percus-Yevick (PY) model due to the hard sphere double Yukawa potential (HSDY) in the framework of the random phase approximation (RPA) [28–30].

SAXS curves of LNPs have been modeled by the form factor of a barrel formed by the stacking of polydisperse CP platelets [31,32] covered with a non continuous layer of P80 with low surface density. The stacking structure factor has been described in the framework of the para-crystal theory [33–36]. The excess P80 molecules of these samples are considered to form micelles, described with the same approach used for samples of only P80.

In the following paragraphs, a complete description of these models is shown.

SAXS of growing and interacting end-capped cylindrical micelles Micelles composed by the nonionic surfactant P80 are supposed to be distributed in different sizes according to the ladder model derived by Thomas et al. [27]. We first consider the chemical potential of a micelle formed by m self-assembled molecules, $\mu_m = \mu_m^\circ + \mathrm{R}T \log C_m$, where R is the perfect gas constant, T the absolute temperature, C_m the molar concentration of the micelle and μ_m° is the standard chemical potential in the molar unit (corresponding to $C_m = 1$ M). The formation of this micelle from m isolated molecules is written as a chemical reaction, $m\,\mathrm{P80} \rightleftharpoons \mathrm{P80}_m$. At the equilibrium, according to standard thermodynamics, the chemical potential of P80 in any state should be the same, hence $\mu_1 = \mu_m/m$. It follows that $C_m = C_1^m e^{-(\mu_m^\circ - m\mu_1^\circ)/(\mathrm{R}T)}$. The ladder model [27] simply assumes that the standard chemical potential difference, $\mu_m^\circ - m\mu_1^\circ$, is a linear function of m,

$$\mu_m^\circ - m\mu_1^\circ = \Delta + (m - m_0)\delta \tag{1}$$

where Δ is the free energy gain when a micelle with the minimum aggregation number m_0 is formed and δ is the free energy gain when a molecule is added to a micelle already formed. To note, both Δ and δ must be negative, indicating that the two corresponding processes are favored. On the other hand, $\Delta - m_0\delta$, the free energy required

Table 1
Chemical groups forming the polar and the hydrophobic domains of CP and P80 molecules. The first block of the table reports the number of electrons and the molecular volume at 25 °C of each group. The second bloc reports the abundance of the groups in the hydrophobic and polar domains CP and P80 molecules. [(a)] Data calculated according to Marsh et al. [37].

	> C =	= O	–O–	OH	CH	CH_2	CH_3	H_2O
n. electrons	6	8	8	9	7	8	9	10
v° [(a)] (Å^3)	13.0	12.0	15.0	16.0	21.5	27.7	52.9	29.9
CP polar head	1	1	1					
CP hydrophobic tail						29	2	
P80 dry polar head	1	1	22	3	4	42		
P80 hydrophobic tail					2	14	1	

to form two end-caps in the cylindrical body of the micelle should be positive. The mass balance of P80 leads to the following equation, $C_{P80} = C_1 + \sum_{m=m_0}^{\infty} mC_m$, where $C_{P80} = c_{P80}\, d_{wat} / M_{P80}$ is the nominal molar concentration of P80 (c_{P80} is the w/v concentration at the reference temperature $T_\circ = 298.15$ K, M_{P80} is the molecular weight of P80 and d_{wat} is the bulk water relative mass density, calculated, according to Eq. (2) of Spinozzi et al. [30], as a function of T). We thus derive $C_{P80} = C_1 + e^{-(\Delta - m_0\delta)/(RT)} \sum_{m=m_0}^{\infty} mC_1^m e^{-m\delta/(RT)}$. The last equation can be re-written in terms of the fraction of free P80 molecules in solution, $\alpha_1 = C_1/C_{P80}$, and by calculating the derivative of the sum of the first m elements of a geometric series. The result leads to an equation of the unique variable $z = \alpha_1 C_{P80} e^{-\delta/(RT)}$,

$$z e^{\delta/(RT)} + e^{-(\Delta - m_0\delta)/(RT)} z^{m_0} \frac{m_0 - z(m_0 - 1)}{(1-z)^2} = C_{P80} \tag{2}$$

We have checked that, by assuming $z < 1$, Eq. (2) can by numerically solved. As a result, the fraction α_1 can be obtained as a function of c, T and the two thermodynamic parameters ruling the micellar processes, Δ and δ. Moreover, the average micellar aggregation number, $<m>$, can be easily derived, according to Eq. S10 of the SM. Examples of numerical solutions of Eq. (2) and calculation of C_m are shown in Fig. S1 of the SM. By extending this treatment from a discrete to a continuous approach and by neglecting the SAXS contribution of isolated P80 molecules, the average form factor of end-cap cylindrical (ec) micelles can be written by

$$P_{ec}(q) = \int_{m_0}^{\infty} p(m) P_{ec,m}(q)\, dm \tag{3}$$

where $P_{ec,m}(q)$ is the form factor of the micelle formed by the aggregation of m P80 molecules of which m_0 are involved in the formation of two end-caps and the remaining $m - m_0$ are forming a cylindrical region between them and $p(m)$ represents the probability density of having micelles with m molecules,

$$p(m) = \frac{C_m}{\int_{m_0}^{\infty} C_m\, dm}. \tag{4}$$

An expression similar to Eq. (3) can be derived for the average amplitude of polydisperse micelles,

$$P_{ec}^{(1)}(q) = \int_{m_0}^{\infty} p(m) P_{ec,m}^{(1)}(q)\, dm \tag{5}$$

We have adopted one of the most suitable SAS models for describing this kind of micellar shape [38], which is the one developed by Kaya [26], here extended to the presence of an inner hydrophobic domain (2-domain) and an outer hydrated polar head domain (1-domain). A representation of this model is shown in Fig. 2. The geometrical parameters of the model are the radius $R_{2,cyl}$ (green segment, Fig. 2) of the inner cylindrical domain (intense blue shadow, Fig. 2) and its length L (dark-green segment, Fig. 2), the thickness δ_{cyl} (orange segment, Fig. 2)

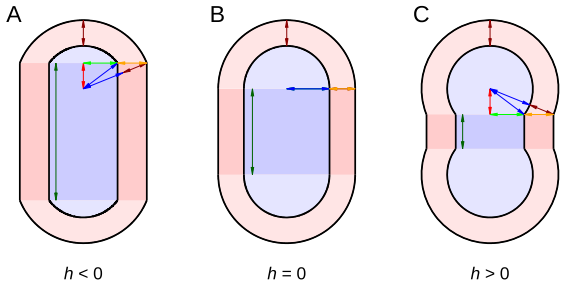

Fig. 2. Sketches of the globular end-cap cylinder model, with negative, null and positive parameter h, panels A, B and C, respectively. The geometrical parameters of the model represented with colored segments, are: h (red, absolute value), $R_{2,cyl}$ (green), $R_{2,cap}$ (blue), δ_{cyl} (orange), δ_{cap} (dark-red) and L (dark green). Areas with less intense and more intense shadings represent the ED of end-cap and cylindrical regions, respectively, red and blue shading being the corresponding hydrated polar head and hydrophobic domains, respectively. (For interpretation of the colors in the figure(s), the reader is referred to the web version of this article.)

of the outer cylindrical shell (intense red shadow, Fig. 2), the radius $R_{2,cap}$ (blue segment, Fig. 2) of the inner spherical cap domain (less intense blue shadow, Fig. 2) and the thickness δ_{cap} (dark-red segment, Fig. 2) of the outer shell of the spherical cap domain. The parameter $h = \pm\sqrt{R_{2,cap}^2 - R_{2,cyl}^2}$ (red segment, Fig. 2) could be negative, null, or positive, as highlighted in panels A-C of Fig. 2, respectively. To note, the condition $R_{2,cap} > R_{2,cyl}$ should be respected. By observing the right triangles with the colored sides that appear in panels A and C of Fig. 2, it is evident that $\delta_{cyl} + R_{2,cyl} = \sqrt{(R_{2,cap} + \delta_{cap})^2 - h^2}$, hence only one of two parameters δ_{cyl} and $R_{2,cyl}$ can be considered independent. The scattering parameters of the model are the electron densities (EDs) of the cylindrical and end-cap regions, distinguished in hydrated polar domains ($\rho_{1,cyl}$ and $\rho_{1,cap}$, more intense and less intense red shadows in Fig. 2) and in hydrophobic domains ($\rho_{2,cyl}$ and $\rho_{2,cap}$, more intense and less intense blue shadows in Fig. 2). The geometrical parameters of the model can be related to the aggregation numbers m and m_0. Indeed, by referring to the hydrophobic molecular volume of P80 in the end-cap domain, $v_{hyd,cap}$, we have the following constraint,

$$m_0 v_{hyd,cap} = \frac{4}{3}\pi R_{2,cap}^3 \left[1 + \frac{3}{2}\frac{h}{R_{2,cap}} - \frac{1}{2}\left(\frac{h}{R_{2,cap}}\right)^3\right], \tag{6}$$

whereas, considering the hydrophobic molecular volume of P80 in the cylindrical domain, $v_{hyd,cyl}$, we have

$$(m - m_0) v_{hyd,cyl} = \pi R_{2,cyl}^2 L \tag{7}$$

The X-ray scattering amplitude $A_m(\mathbf{q})$, which is defined as the Fourier transform of the excess X-ray scattering length density, of the core-shell end-cap cylinder formed by m P80 molecules, derived according to Kaya's model [26], is fully reported in Eq. S11 of the SM as a function

of the components of the scattering vector **q** parallel and perpendicular to the cylindrical axis, $q_{\parallel} = q\cos\beta_q$ and $q_{\perp} = q\sin\beta_q$, respectively (β_q is the angle between **q** and the cylindrical axis and q is the modulus of **q**). Corresponding orientational integrals $P_{\mathrm{ec},m}(q)$ and $P^{(1)}_{\mathrm{ec},m}(q)$ are defined in Eqs. S16 and S17 of the SM. By entering the results of the ladder model, $C_m = e^{-(\Delta - m_0\delta)/(RT)}e^{-mE}$, where the positive dimensionless parameter $E = \delta/(RT) - \log C_{\mathrm{P80}} - \log\alpha_1$ has been introduced, we have been able to simplify Eqs. (3) and (5) according to

$$P_{\mathrm{ec}}(q) = \int_0^{\pi/2} d\beta_q \sin\beta_q \frac{N_2}{D_2}, \tag{8}$$

$$P^{(1)}_{\mathrm{ec}}(q) = \int_0^{\pi/2} d\beta_q \sin\beta_q \frac{N_1}{D_1}, \tag{9}$$

where the working factors N_2, D_2, N_1 and D_1 are fully reported in Eqs. S18-S21 of the SM. The volumetric properties of the P80 molecules have been used to calculate all the electron densities as well as the area per molecule in both end-cap and cylinder regions. All details are shown in Sect. S11.2 of the SM. Besides, the average number density of the micelles, defined by $n_{\mathrm{ec}} = N_A\int_{m_0}^{\infty} C_m\, dm$ (N_A is Avogadro's number), is $n_{\mathrm{ec}} = (N_A/E)e^{-(\Delta - m_0\delta)/(RT) - m_0 E}$.

The effective structure factor $S_M(q)$, a term that reflects the correlation among micelles, particularly relevant at the high concentration (particle volume fraction η greater than ≈ 0.01), and that depends on the coupling function $\beta(q) = [P^{(1)}_{\mathrm{ec}}(q)]^2/P_{\mathrm{ec}}(q)$ [30], is modeled with the same approach, based on the HSDY potential, that some of us have successfully applied to different nanosized systems [39,30,40]. In the case of the nonionic P80 surfactant, the micelle charge is set to zero. Hence, the only relevant parameters are the effective average micelle diameter σ_{ec} (so that the volume fraction that appears in the PY expression of $S_0(q)$ (see Eq. S1 of Piccinini et al. [40]) is $\eta = n_{\mathrm{ec}}\pi\sigma^3_{\mathrm{ec}}/6$), the depth J of the attractive potential's well, and the decay range d. Moreover, since our experimental data show a q^{-4} behavior at low q (Sect. 3.3) probably due to the presence of very large micellar aggregates, the final equation used to fit all the experimental SAXS differential macroscopic cross section recorded for the samples containing only P80 is

$$\frac{d\Sigma}{d\Omega}_{\mathrm{ec}}(q) = n_{\mathrm{ec}}r_e^2 P_{\mathrm{ec}}(q)S_M(q) + k_{\mathrm{por}}q^{-4} \tag{10}$$

where k_{por} represents the Porod's constant. The factor $r_e = 0.28\cdot 10^{-12}$ cm is the scattering length of the electron.

SAXS of stacked polydisperse platelets in the form of barrel SAXS data of CP solid LNPs stabilized by P80 (Sect. 3.3) show two sets of low-order diffraction peaks, similar to previous results [41–43,21,44,20,6], that grow over a typical bilayer band, widely seen in SAXS experiments of flat bilayers [45], suggesting the presence of platelets. The first peak's positions of the two families are at ≈ 0.160 Å^{-1} and ≈ 0.143 Å^{-1}, corresponding to repeat distances of ≈ 39.3 Å and ≈ 43.9 Å, respectively. The low q behavior of these SAXS curves shows a power trend q^{-p} with exponent $2 < p < 3$, far from the characteristic $p = 2$ value of freely rotating platelets in solution [46], indicating that a certain degree of parallel platelet-platelet stacking interaction would occur. Based on these preliminary observations, together with the AFM and DLS results shown in Sect. 3 and by taking into account the detailed model developed by Schmiele et al. [31,32] for platelet systems, we have worked out a novel model aimed at analyzing SAXS curves in the whole q-range. As a matter of fact, it should be noted that no model among those reported in the literature has proved capable of fitting the SAXS curves in the entire range of q. This novel model (Fig. 3A) is based on the following assumptions.

(i) The platelets are composed of three cylindrical structures that are embedded inside one another (Fig. 3B). The innermost cylinder (blue,

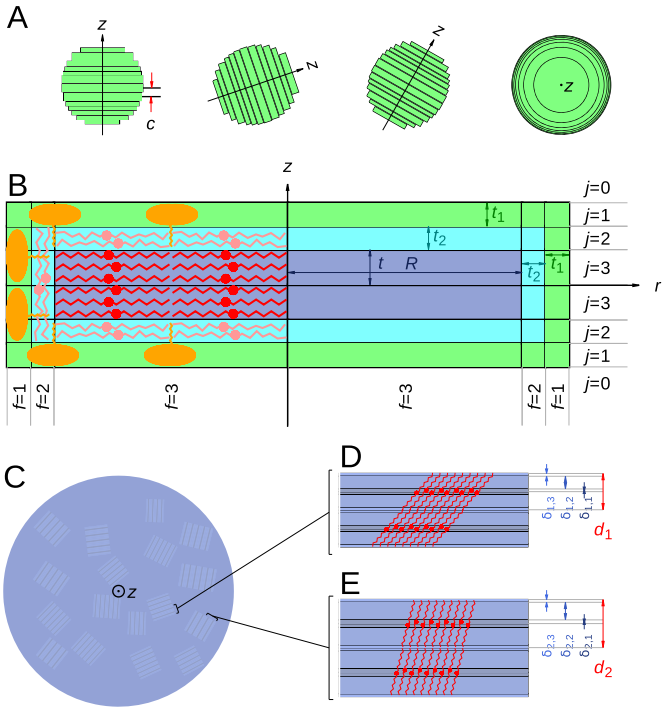

Fig. 3. The platelets model for LNPs. A) Randomly oriented, polydispersed, barrel-like LNPs. Each comprises a stack of N_c platelets, orthogonal to their main axis z, separated by a distance c (red marks), with N_c and c following Gaussian distributions and a cross-section radius distributed according to an elliptical profile (Fig. S2). B) Section of a single platelet along its central axis z. The inner cylinder (blue), made of crystalline CP molecules (red), has half-height t and radius R (vertical and horizontal dark-blue double arrows, respectively). The t/R ratio is not in scale and has been chosen for the sake of visualization. Amorphous-CP molecules (pink) form a cylindrical shell (cyan) with thickness t_2 (dark-cyan double arrows) within another cylindrical shell (green) with thickness t_1 (dark-green double arrows) made of P80 molecules (orange) and bound water (not shown). Labels $f = 1$, 2, and 3 mark the regions with different ED profiles along z. The $f = 3$ region has six layers ($j = 1$, 2, 3, and those specular to the central plane orthogonal to z, with thicknesses t_1, t_2, and t, respectively) with distinctive EDs. The $f = 2$ region has layers $j = 2$ and 3 with the same ED, while for the $f = 1$ region all the layers have the same ED. C) Cross section of the inner cylinder (outgoing z axis) in which small crystalline domains, randomly oriented and containing several parallel CP bilayers, are shown. The crystalline domains are distinguished into two groups, with shorter and longer lamellar distances. A zoom of two adjacent bilayers for each of the two groups of crystalline domains is shown in panels D and E, respectively, where the red double arrows represent the corresponding lamellar distances d_1 and d_2. A hypothetical disposal of the CP molecules, oriented differently in the two types of bilayers, is shown. The three specular layers, shown by decreasing intensities of blue, represent the ED of the carboxyl group, the middle and terminal chains, respectively. Their corresponding thicknesses $\delta_{k,1}$, $\delta_{k,2}$ and $\delta_{k,3}$ ($k = 1, 2$) are indicated by the double arrows shown on the right with the same color as the ED domains.

Fig. 3C) is made up of lamellar layers consisting of CP molecules (red) with internal structures (Fig. 3D and E). This cylinder is surrounded by a cylindrical shell (cyan) consisting of widely-spaced P80 aliphatic chains (orange) and amorphous CP molecules (pink). The outer cylinder (green) is made up of P80 polar heads and bound water molecules that bridge the hydrophilic moieties, as illustrated in atomistic simulations of phospholipid membranes [47].

(ii) The innermost cylinder (shown in Fig. 3 in blue color) has both the radius R and the height $2t$ polydisperse. The mean value of the radius is indicated with $R_0 = \langle R\rangle$, its dispersion index is $\xi_R = (\langle R^2\rangle - R_0^2)^{1/2}/R_0$, while $t_0 = \langle t\rangle$ indicates the mean value of half the height of the inner cylinder, with dispersion index $\xi_t = (\langle t^2\rangle - t_0^2)^{1/2}/t_0$.

(iii) According to AFM results, we assume that LNPs are barrel-shaped particles, defined by a maximum and a minimum radius of the circular cross-section, R_M and $R_m = \nu R_M$, respectively, with $0 < \nu < 1$, ν being the "bulging" parameter of the barrel. Also, we assume a smooth variation of the barrel's circular cross-section radius according to an elliptical profile, as depicted in Fig. S2 of the SM, where we have also plotted the theoretical distribution function of the barrel circular cross-section radius,

$$p(R, R_M, R_m) = \begin{cases} \frac{R - R_m}{(R_M - R_m)\sqrt{(R_M - R)(R_M + R - 2R_m)}} & R_m \le R < R_M \\ 0 & \text{otherwise} \end{cases} \quad (11)$$

According to this view, the barrel shape is obtained by the stacking of parallel cylindrical platelets (Fig. 3A). Since AFM results indicate a polydispersion of the barrel size, we assume a Gaussian distribution of the maximum circular cross-section radius R_M of the barrel, centered at $R_{M,\max}$ and with standard deviation $\xi_{R_M} R_{M,\max}$, As a consequence, the overall distribution function $p(R)$ of the platelet radius is written as,

$$p(R) = \int_{R_{M,\text{lb}}}^{R_{M,\text{ub}}} p(R, R_M, \nu R_M)\, p(R_M)\, d R_M \quad (12)$$

$$p(R_M) = \frac{1}{Z_{R_M}} e^{-(R_M - R_{M,\max})^2 / (2\xi^2_{R_M} R^2_{M,\max})} \quad (13)$$

The lower and the upper bounds of the integral are $R_{M,\text{lb}} = \max\{R_{M,\max}(1 - p_G \xi_{R_M}), R_{M,\min}\}$ and $R_{M,\text{ub}} = R_{M,\max}(1 + p_G \xi_{R_M})$, respectively, where $p_G \approx 3$ represents the number of standard deviations of the Gaussian taken into consideration, whereas $R_{M,\min}$ represents the minimum value of R_M, a parameter necessary in order to avoid non-physical negative values of R_M. The normalization factor, Z_{R_M}, can be analytically calculated as reported in Eq. S22 of the SM. Examples of $p(R)$ calculated with Eq. (13) are reported in Fig. S3 of the SM. To note, the average platelet radius and its dispersion are calculated according to

$$R_0 = \int_{\nu R_{M,\text{lb}}}^{R_{M,\text{ub}}} R\, p(R) d R \quad (14)$$

$$\xi^2_R = \frac{1}{R^2_0} \int_{\nu R_{M,\text{lb}}}^{R_{M,\text{ub}}} (R - R_0)^2\, p(R)\, d R \quad (15)$$

with $\int_{\nu R_{M,\text{lb}}}^{R_{M,\text{ub}}} p(R)\, d R = 1$. Analytical expressions of R_0 and ξ_R are given in Eqs. S23-S24 of the SM.

(iv) A Gaussian function also describes the distribution function of t with the maximum at the position $t_{\max}$ and the standard deviation defined as $\xi_{t_{\max}} t_{\max}$. Since t is a positively defined quantity, the average thickness, t_0 and the dispersion, ξ_t, are calculated by integrating the Gaussian function only in a positive range of t, as described in detail in the Sect. S5 of the SM. To note, t is represented by a dark-blue arrow in Fig. 3B.

(v) Platelets are highly anisometric cylinders, with $R \gg t$, hence, according to scattering theory [46], the SAXS signal only depends on the excess ED along the axis z of the platelet (drawn in Fig. 3B). As a consequence, there are three distinct ED profiles along z, indicated with the label $f = 1, 2, 3$, each of them formed by 3 specular layers in respect to the middle plane orthogonal to the z axis (Fig. 3B). Such layers are indexed by $j = 1, 2, 3$, and the corresponding thicknesses are t_1, t_2 and t. In positions labeled with $j = 0$ in Fig. 3B there are stacked platelets with their t_1, t_2 and t layers, with a stacking interlayer distance $\Delta t \simeq 1$ Å, as discussed in section 3.3.2 (Fig. 9M). We associate $\Delta t/2$ to each stacked platelet as a correction to the thickness t_1 of the hydrated-P80 layer. For the ED profile indexed with $f = 3$, the 3 layers have distinct values of ED, as shown in Fig. 3 with blue ($j = 3$), cyan ($j = 2$) and green ($j = 1$) colors. Differently, for the ED profile with index $f = 2$, two layers have the same ED, shown in cyan ($j = 2, 3$) in Fig. 3B, whereas for $f = 1$ all layers have the same ED. We also assume smooth transitions of EDs from two subsequent layers and from the last layer to bulk water by adopting the error function to describe the smooth effect (see Fig. S4 of the SM and Spinozzi et al. [48] for details). The smooth parameter from j-layer to $(j-1)$-layer is the standard deviation $\sigma_{\text{pl},j}$ of the error function.

(vi) The stacking among roughly parallel platelets (Fig. 3A) is described by the para-crystal theory applied along the z direction, with a repeat distance $c = 2(t + t_2 + t_1 + \Delta t/2)$ (Fig. 3A, red arrows) and distortion parameter $g_c = \sigma_c/c$, σ_c being the standard deviation of c. The number of stacking platelets, N_c, is polydisperse, according to a Gaussian distribution function $p_{N_c}(N_c)$, with the maximum at the position $N_{c,\max}$ and the standard deviation indicated with σ_{N_c}. Since N_c cannot be negative, the average para-crystal structure factors, as well as the average number of platelets, $N_{c,0}$, are calculated by integrating the Gaussian distribution function only in a positive range of N_c, as detailed in the Sect. S6 of the SM.

(vii) The CP molecules in the innermost cylinder (Fig. 3C) are organized into three groups, two of which correspond to two nano-sized lamellar domains (Fig. 3D and E) and the third group forming an amorphous domain. The molar fraction of CP in the three groups are named y_k, with the obvious condition $\sum_{k=1}^{3} y_k = 1$. The lamellar orders of the domains (ld) are described by the para-crystal scheme of Frühwirth et al. [49], defined by the repetition distance d_k (Fig. 3D and E, red arrows), the distortion $g_{\text{ld},k}$ and the average repeat number $N_{\text{ld},k}$, with $k = 1, 2$. In turn, the repetition distance is $d_k = 2(\delta_{k,1} + \delta_{k,2} + \delta_{k,3})$, where $\delta_{k,i}$ is the thickness of the i-layer of ED corresponding to the carboxyl group, the middle, and the terminal chains of the CP molecules, with $i = 1, 2, 3$, respectively (see arrows with decreasing intensity of blue in Fig. 3D and E). Smooth transitions from i-layer to $(i-1)$-layer are modeled based on the error function with standard deviation $\sigma_{k,i}$. To note, the 0-layer has the ED corresponding to the average of the EDs of the three layers, as shown in Fig. S5 and Eq. S61 of the SM and Ref. Spinozzi et al. [48].

(viii) The P80 molecules are divided into two groups. Those in the first group (with molar fraction y_{P80}) are distributed on the platelets' surface, with their large polar head in the layer $j = 1$ and their hydrophobic chain in the intermediate layer ($j = 2$), among the CP molecules considered in amorphous configuration (Fig. 3B). The polar heads of P80 molecules are hydrated by bound water in the $j = 1$ layer. As discussed in Sect. 3.3.2, the bound water is responsible for the collapse of the platelets. The second group of P80 molecules, with a molar fraction $1 - y_{\text{P80}}$, consists of all the molecules forming end-cap cylinder micelles, according to the model described in the Sect. 2.2.4, paragraph "SAXS of growing and interacting end-capped cylindrical micelles". However, as discussed in Sect. 3.3, we found that $y_{\text{P80}} = 1$. Hence, there are no end-cap cylinder micelles in the LNPs, although the general theory includes them.

(ix) Both the height of the barrel, $H = c\, N_c$, and the circular cross-section radius of the barrel, R, are considered larger than $\approx 1/q_{\min}$, $q_{\min}$ being the minimum modulus of the scattering vector detectable by SAXS experiments. Hence, the contribution of the whole barrel to the SAXS signal depends on the average surface of the barrel and is due to the excess ED of all the molecules within the barrel (CP, P80 and bound water between the platelets) with respect to the bulk water, a case similar to that described by Porod's law. To note, in the case of a barrel-like LNP that interacts with other molecules, such as proteins, the SAXS contribution of the barrel surface will be approximated by the form factor of N_s layers of different EDs in planar geometry, with possible smooth transitions, according to the classical scattering theory [46]. The distribution function of H corresponds to $p(H) = (1/c) p_{N_c}(H/c)$. We have also developed a simple Monte Carlo method to derive the distribution function of the center-to-border distance of the barrel, $p(R_c)$, by com-

bining the distributions functions $p(R_M)$ and $p(H)$. Details are given in the Sect. S7 of the SM.

We will now derive the SAXS differential macroscopic cross section of platelets according to all these assumptions, from (i) to (ix). According to scattering theory [46], the SAXS differential macroscopic cross section of flat (fl), thin and not interacting (ni) platelet with surface S_{fl} and number density n_{pl} is

$$\frac{d\Sigma}{d\Omega}_{\mathrm{fl,ni}}(q) = n_{\mathrm{pl}} r_{\mathrm{e}}^2 \frac{2\pi}{q^2} S_{\mathrm{fl}} |A_{\mathrm{fl}}(q)|^2 \tag{16}$$

where $A_{\mathrm{fl}}(q) = \int \delta\rho(z) e^{iqz} dz$ is the Fourier transform the excess ED profile $\delta\rho(z)$ along the direction z perpendicular to the platelet. The number density of platelets, n_{pl}, with inner radius R, half-inner length t and shell thicknesses t_1 and t_2 can be calculated considering the CP w/v concentration, c_{CP}, by $n_{\mathrm{pl}} = N_A c_{\mathrm{CP}} / (M_{\mathrm{CP}} N_{\mathrm{CP,pl}})$, where M_{CP} is the CP molecular weight and $N_{\mathrm{CP,pl}}$ is the number of CP molecules in the platelet, which can be derived on the basis of the mass balance, as shown in Eq. S105 of the SM. By referring to assumption (v), since for platelets we have three ED profiles along z ($f = 1, 2, 3$), the differential macroscopic cross section of the platelets is

$$\frac{d\Sigma}{d\Omega}_{\mathrm{pl,ni}}(q) = n_{\mathrm{pl}} r_{\mathrm{e}}^2 \frac{2\pi}{q^2} \Big[\pi((R+t_2+t_1)^2 - (R+t_2)^2) A_{\mathrm{fl},1}^2(q) + \pi((R+t_2)^2 - R^2) A_{\mathrm{fl},2}^2(q) + \pi R^2 A_{\mathrm{fl},3}^2(q) \Big] \tag{17}$$

The real functions $A_{\mathrm{fl},f}(q)$ for specular layers with smooth transitions based on error functions are reported in Eq. S44 of the SM. By substituting the expression of $N_{\mathrm{CP,pl}}$ shown in Eq. S105 of the SM and considering both the polydispersion model described in assumption (ii) and the stacking correlation described in assumption (vi), the differential macroscopic cross section of interacting (in) polydisperse platelets, averaged over R and t (av), is

$$\frac{d\Sigma}{d\Omega}_{\mathrm{pl,in,av}}(q) = r_{\mathrm{e}}^2 \phi_{\mathrm{CP}} \left(1 + \frac{\nu_{\mathrm{P80,hyd}} y_{\mathrm{P80}}}{\bar{\nu}_{\mathrm{CP}} r_{\mathrm{CP,P80}} k_{r_{\mathrm{CP,P80}}}} \right) \times \frac{\pi}{q^2} \Big(< t_1(t_1 + 2(R+t_2))(R+t_2)^{-2} >_R < (t+t_2)^{-1} A_{\mathrm{fl},1}^2(q) >_t + < t_2(t_2+2R)(R+t_2)^{-2} >_R < (t+t_2)^{-1} A_{\mathrm{fl},2}^2(q) >_t + < R^2 (R+t_2)^{-2} >_R < (t+t_2)^{-1} A_{\mathrm{fl},3}^2(q) >_t \Big) S_{\mathrm{pl}}(q) \tag{18}$$

where $\phi_{\mathrm{CP}} = N_A c_{\mathrm{CP}} \bar{\nu}_{\mathrm{CP}} / M_{\mathrm{CP}}$ (see Eq. S109 of the SM) is the overall CP volume fraction, $r_{\mathrm{CP,P80}}$ is the nominal molar ratio between CP and P80 molecules, with an eventual correction factor and $k_{r_{\mathrm{CP,P80}}}$. The terms $\nu_{\mathrm{P80,hyd}}$ and $\bar{\nu}_{\mathrm{CP}}$ are the volumes of the hydrophobic tail of P80 and the mean volume of CP, as detailed in Eq. S66 and S108 of the SM, respectively. The radial averages ($< \cdots >_R$) are calculated on the basis of the function $p(R)$, as shown in Eq. S52 of the SM. The t-averages $< (t+t_2)^{-1} A_{\mathrm{fl},f}^2(q) >_t$ are determined as fully described in Eq. S47 of the SM. The factor $S_{\mathrm{pl}}(q)$ in Eq. (18) represents the platelet-platelet structure factor, which is calculated according to para-crystal order along the z direction. The expressions can be found in literature [49,48].

Regarding the SAXS differential macroscopic cross sections of the two groups of randomly oriented nano-sized lamellar domains (ld) of CP within the inner cylinder, foreseen by assumption (vii), according to scattering theory it can be shown that they are two terms that add up to the one due to the platelets since the average cross-terms between the cylindrical layer of the platelets, and the nano-domains drop to zero. Considering the stacks of flat bilayers, as shown in Fig. 3D and E, their differential macroscopic cross section is

$$\frac{d\Sigma}{d\Omega}_{\mathrm{ld,in}}(q) = r_{\mathrm{e}}^2 \phi_{\mathrm{CP},3} \frac{2\pi}{q^2} \sum_{k=1}^{2} \frac{y_k}{d_k} A_{\mathrm{ld},k}^2(q) S_{\mathrm{ld},k}(q) \tag{19}$$

where $\phi_{\mathrm{CP},3}$ is the volume fraction of CP in the inner region of the platelets (see Eq. S110 of the SM) and $A_{\mathrm{ld},k}(q)$ is the Fourier transform of the excess ED profile of the 3-specular layers of the k-nano-domain calculated with respect to the average ED of the CP molecules (represented in blue in Fig. 3). Its expression is given in Eq. S62 of the SM. The stacking between CP k-domains is described by the para-crystal structure factor $S_{\mathrm{ld},k}(q)$.

The SAXS contribution due to the overall barrel-like surface, based on the assumption (ix), is

$$\frac{d\Sigma}{d\Omega}_{\mathrm{brl}}(q) = n_{\mathrm{brl}} r_{\mathrm{e}}^2 \frac{2\pi}{q^2} < S_{\mathrm{brl}} > |A_{\mathrm{brl}}(q)|^2 \tag{20}$$

where n_{brl} is the average number density of barrels (see Eq. S123 of the SM), $< S_{\mathrm{brl}} >$ is the average barrel surface (calculated according to Eq. S132 of the SM) and $A_{\mathrm{brl}}(q)$ is the Fourier transform of the excess ED profile along the direction perpendicular to the barrel surface, fully described in Eq. S138 of the SM. It can be easily shown that the scattering cross-term between the barrel and the platelets has a mean value that tends to be zero.

The final equation used to fit the SAXS data of LNP samples, which includes all the assumptions (i)-(ix) is the sum of Eqs. (18), (19), (20) and (10),

$$\frac{d\Sigma}{d\Omega}_{\mathrm{LNP}}(q) = \frac{d\Sigma}{d\Omega}_{\mathrm{pl,in,av}}(q) + \frac{d\Sigma}{d\Omega}_{\mathrm{ld,in}}(q) + \frac{d\Sigma}{d\Omega}_{\mathrm{brl}}(q) + \frac{d\Sigma}{d\Omega}_{\mathrm{ec}}(q) \tag{21}$$

where in the term $\frac{d\Sigma}{d\Omega}_{\mathrm{ec}}(q)$ (Eq. (10)), which accounts for the SAXS contribution of P80 molecules that are not involved in the platelets, the number density of end-cap cylindrical micelles, n_{ec}, is calculated as widely described in Sec. 2.2.4, paragraph "SAXS of growing and interacting end-capped cylindrical micelles", and considering the available molar concentration of P80 as large as $C_{\mathrm{P80}} = c_{\mathrm{P80}}(1 - y_{\mathrm{P80}}) d_{\mathrm{wat}} / M_{\mathrm{P80}}$.

Global-fit Considering the interplay between the SAXS models introduced in Sect. 2.2.4, paragraphs "SAXS of growing and interacting end-capped cylindrical micelles" and "SAXS of stacked polydisperse platelets in the form of barrel", all SAXS curves of samples containing only P80 and samples of LNP (containing both P80 and CP) can be analyzed by a unique optimization procedure, referred to as global-fit [25]. All model parameters are divided into two classes: the first-class includes the common parameters, such as the volumes of chemical groups, which are optimized to a single value for all curves; the second-class includes single-curve parameters, which can assume an independent value for each curve. The merit function to be minimized is

$$\mathcal{H} = \chi^2 + \alpha L. \tag{22}$$

In this equation, the term χ^2 is the standard reduced chi-square of all the N_v experimental SAXS curves,

$$\chi^2 = \frac{1}{N_v} \sum_{v=1}^{N_v} \frac{1}{N_{q,v}} \sum_{j=1}^{N_{q,v}} \left(\frac{\frac{d\Sigma}{d\Omega}_{v,\mathrm{ex}}(q_j) - \frac{d\Sigma}{d\Omega}_{v,\mathrm{th}}(q_j)}{\sigma_v(q_j)} \right)^2, \tag{23}$$

where $N_{q,v}$ is the number of q-points of the v-curve, $\frac{d\Sigma}{d\Omega}_{v,\mathrm{ex}}(q_j)$, $\sigma_v(q_j)$ is the experimental standard deviation and $\frac{d\Sigma}{d\Omega}_{v,\mathrm{th}}(q_j)$ is the fitting curve calculated based on either Eq. (10) or Eq (21), depending on the kind of sample (s = P80 or s = LNP). The second term, L, is the regularization factor aimed to reduce unlikely oscillations of single-curve parameters related to samples with the closest chemical-physical conditions (composition, concentration, and temperature). The term L is indeed defined by

$$L = \sum_{s=\mathrm{P80,LNP}} \sum_{p=1}^{N_{p,s}} \sum_{v=1}^{N_v} \left(1 - \frac{X_{p,v}}{X_{p,v'}} \right)^2, \tag{24}$$

where the index s in the first sum distinguishes the kind of sample, the index p is the label of the p^{th} of the $N_{p,s}$ single-curve fitting parameters,

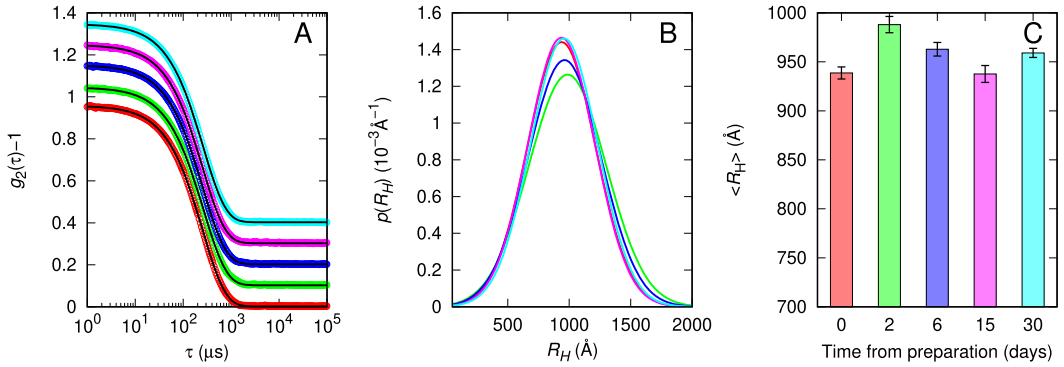

Fig. 4. DLS results of LNPs. A) Auto-correlation functions of LNP recorded at 0 (red), 2 (green), 6 (blue), 15 (magenta) and 30 (cyan) days after the sample preparation with corresponding best fits (solid black lines). A factor of 0.1 vertically scales data for clarity. B) Distribution functions of the hydrodynamic radius R_H obtained by the best fit of DLS auto-correlation functions. C) Mean particle hydrodynamic radius of the distributions shown in panel B. The color code used in panel B and C is as in panel A.

$X_{p,\upsilon}$ is the value of the parameter used to fit the υ-curve and $X_{p,\upsilon'}$ is the value of the parameter used to fit the υ' curve, which is one of the samples with the closest chemical-physical conditions to the sample of the υ-curve. The closest curve is the one that minimizes the term $(1-C_\upsilon/C_{\upsilon'})^2+(1-T_\upsilon/T_{\upsilon'})^2$, where C_υ is the concentration of either P80 or CP. The minimization of the merit function and the evaluation of the uncertainties of fitting parameters are achieved according to a combination of Simulated Annealing and Simplex methods, as detailed described by Moretti et al. [50]. The constant α in Eq. (22) is fixed to ensure that, at the end of the minimization, the factor αL does not overcome $\approx 10\%$ of the merit function $\mathcal{H}$. The present model has been integrated into the GENFIT software [25].

3. Results and discussion

3.1. DLS

In Fig. 4A, we report the second-order intensity autocorrelation functions of a solid LNP dispersion measured on different days after it was prepared. These functions exhibit a single exponential decay, suggesting that the sample primarily comprises particles of the same size. Accordingly, we analyzed the data with a single Gaussian distribution function of the solid LNP's hydrodynamic radius, R_H, as in Eq. S9 of the SM, and achieved optimal fits (black solid lines in Fig. 4A, with fitting parameters in Table S2 of the SM). We show the resulting hydrodynamic radius distributions in Fig. 4B, and the histogram of the average values $<R_H>$ as a function of time from sample preparation in Fig. 4C. These results indicate that the solid LNP size is stable, with an average hydrodynamic radius of $<R_H>\approx 950$ Å, with rather limited temporal variations (in the order of 2%), and with a dispersion index $\xi_{R_H}\approx 0.3$. Additionally, we found that the particles were slightly negative with a ζ potential of -6.5 ± 0.6 mV, which remained relatively constant throughout the investigation.

3.2. AFM

In Fig. 5A, we show a representative image of tens non-contact mode AFM observations obtained from a solid LNP dispersion diluted to 0.1 g/L. The particles show an elongated, barrel-like shape and are noticeably polydisperse. In Fig. 5B-I, we show magnifications of the images centered on the single particles. The jagged morphology in the region close to the border of AFM images (e.g., Fig. 5G and I) is consistent, at least to some extent, with the presence of an internal structure formed by parallel sheets. As described in the Sect. 2, we determined the distribution function of the center-to-border distance R_c, along different straight lines passing from the center, of ~ 50 particles directly observed by AFM (Fig. 5J). The mean value of R_c is ≈ 912 Å, with a dispersion as large as 0.1, in excellent agreement with the mean hydrodynamic radius $<R_H>$ measured by DLS.

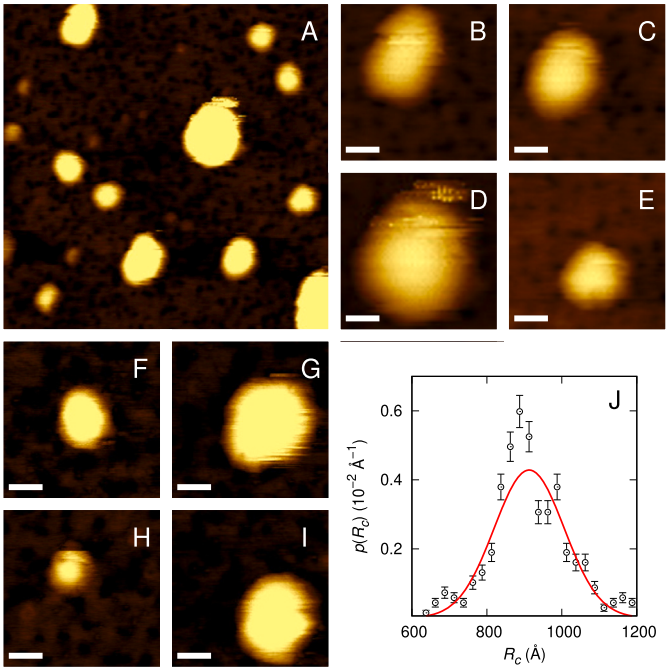

Fig. 5. AFM results for LNPs. Panel A: example image of a sample recorded in non-contact mode. Panels B-I: square magnifications of single LNPs. The bottom horizontal bars span 1000 Å. Panel J: distribution function of the center-to-border distance obtained with ImageJ software [23] by selecting 300 distances measured in random directions passing through the center of 50 individual LNPs. The grid size was 50 Å, and the error bars were assigned according to Poisson statistics. The solid red line represents the best fit through a Gaussian, with the center at 912 ± 6 Å and dispersion 0.100 ± 0.006.

3.3. SAXS

SAXS curves recorded at the ID02 beamline of ESRF for water dispersion for P80 in different concentrations and temperatures are shown in Fig. 6A (semi-logarithmic plot) and B (logarithmic plot), whereas SAXS curves of solid LNPs formed by CP and stabilized by P80 are presented in Fig. 6C (semi-logarithmic plot) and D (logarithmic plot). We show in Fig. S7 of the SM additional SAXS curves, recorded at Austrian SAXS beamline of ELETTRA, for P80 and solid LNPs samples of a second preparation batch but in a more limited number of conditions in terms of concentration and temperature. We analyzed simultaneously

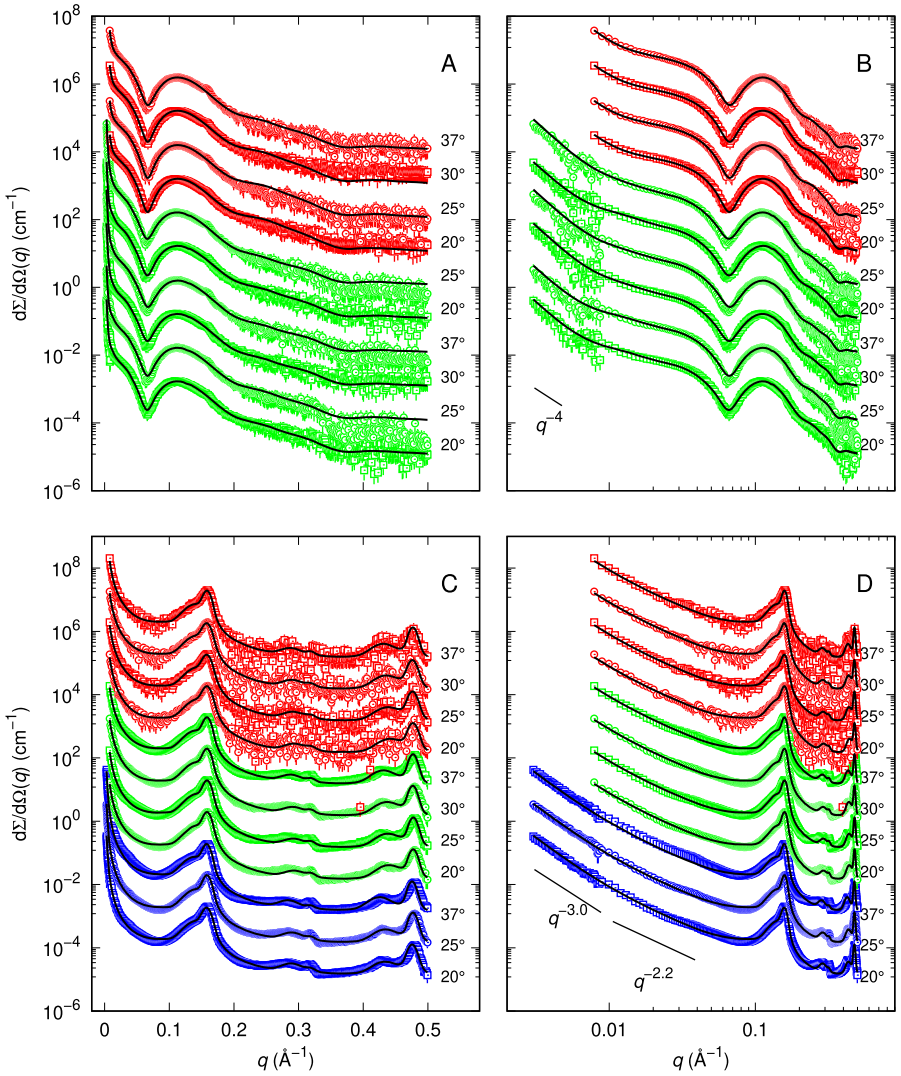

Fig. 6. Synchrotron SAXS curves recorded at the ID02 beamline at ESRF for P80 (panels A-B) and LNP (panels C-D) samples reported in semi-logarithmic plots (panels A and C) and in logarithmic plots (panels B and D), respectively. For a better visualization, curves have been stacked by multiplying for a factor 10^{m-1}, where m is the index of the row from the bottom. In panels A-B, red and green points refer to 13.3 and 1.7 g/L P80 concentration, respectively. In panels C-D, red, green, and blue points refer to 80.0, 40.0, and 1.0 g/L LNP concentration, respectively. Solid black lines are the best fits obtained with the global-fit method.

by a unique calculation, according to the SAXS models fully described in the Sect. 2.2.4, all the P80 and the solid LNP sets of curves recorded at ESRF and ELETTRA. We find that the results for each experimental campaign are very similar. Therefore, we present and discuss here only those from ESRF, while those from ELETTRA are included in the SM.

First, to reduce the number of free fitting-parameters, we duly exploited all the information related to the composition of the molecules P80 and CP, including the volume of the different chemical groups and their dependence on the temperature, to calculate the electron densities of the domains in each of the regions that constitute the end-capped cylindrical micelles (Sect. S11.2 of the SM) and the platelets (Sect. S11.3 of the SM). The parameter y_{P80}, which represents, for the solid LNP samples, the mole fraction of P80 bound to the platelets, was always found equal to 1, indicating that, for these samples, there are no P80 molecules available to form end-cap micelles. To note, the global fit of 21 SAXS curves was obtained by optimizing 16 first-class (common) fitting parameters and 280 second-class (single-curve) fitting parameters (controlled by the regularization method), with an average of 14 parameters per curve. It should be noted that, despite the large number of parameters, the validity range of many of them have been delimited very carefully around known literature values to ensure physical meaning. The first-class fitting parameters, shared among all SAXS curves, and their uncertainties are reported in Table 2.

We show the second-class fitting parameters, together with derived parameters, as a function of temperature for P80 samples (Fig. 7) and solid LNP samples (Fig. 9). The merit function $\mathcal{H}$ at the end of the minimization, resulted 6.4, corresponding to a total reduced χ^2 of 6.1.

3.3.1. Polysorbate 80

The quality of the fits throughout the whole range of q can be appreciated by observing Fig. 6A and B. Considering the single-curve fitting parameters (Fig. 7), we first observe that the inner radius of the two end-caps is ≈ 18 Å (Fig. 7A), slightly depending on temperature and concentration. We find that the parameter h (Fig. 7B) is negative, with a value ≈ −10 Å, and the thickness of the end-cap shell (Fig. 7C) is around 34 Å. These values, the fitted thermodynamic parameters Δ and δ (Table 2) lead to a very spheroidal shape of P80 micelles (Fig. 8).

The derived parameter m_0 (Fig. 7G), corresponding to the number of P80 molecules in the end-cap region, is ≈ 14, very close to the average value $<m>$ from Eq. S10 of the SM. Indeed, the probability densities $p(m)$ of finding micelles with m molecules (Fig. S11 of the SM) is low for $m > m_0$. Therefore, the cylindrical region of the micelles is almost negligible, and the micelle in Fig. 8A is the most representative.

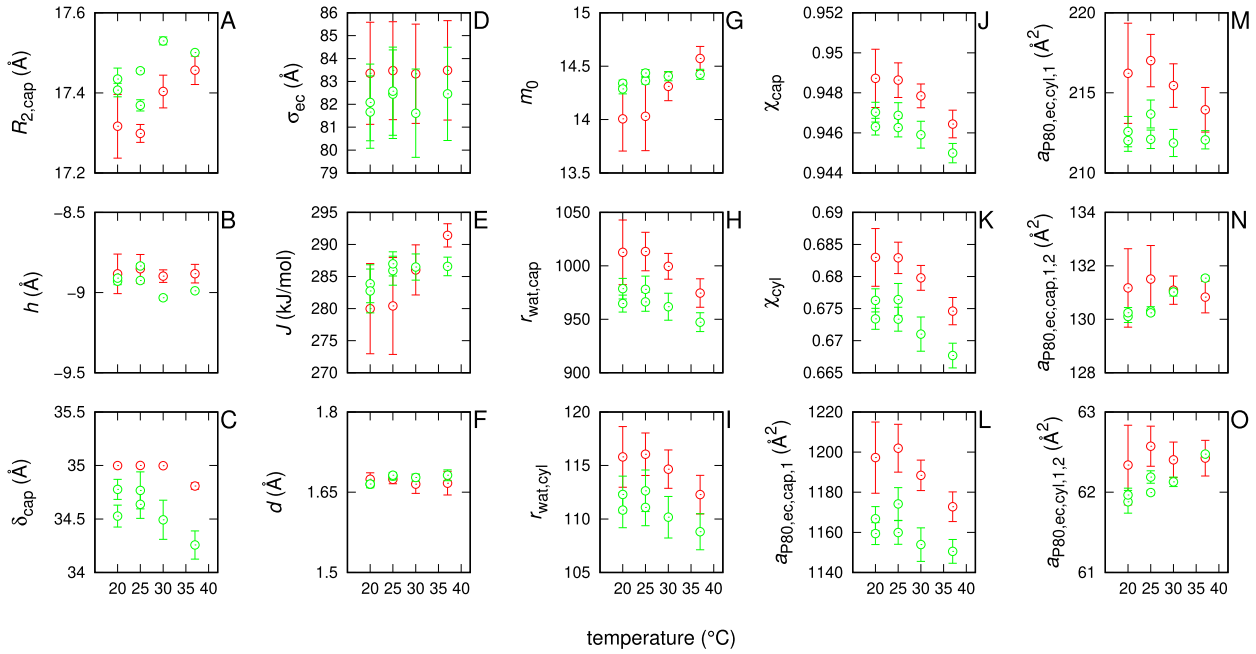

Fig. 7. Second-class fitting parameters (panels A-F) and derived fitting parameters (panels G-O) as from ESRF-SAXS data for P80 (Fig. 6A-B). The parameters and symbols are defined in SM. Red and green points refer to $C_{P80} = 13.3$ and 1.7 g/L, respectively. The validity ranges of the fit parameters shown in the panels are: A) [6,30] Å; B) [-30,30] Å; C) [6,50] Å; D) [0,100] Å; E) [0,500] kJ/mol; F) [0.1,10] Å.

Table 2
First-class fitting parameters for the SAXS data recorded by the ID02 beamline at ESRF. The parameters and symbols are defined in SM. The units of length and volume are Å and Å^3, respectively. Validity ranges of fitting parameters: [a] $[-1000, 1000]$; [b] $[-50, 50]$; [c] [12.0, 15.0]; [d] [11.0, 14.0]; [e] [14.0, 17.0]; [f] [14.0, 17.0]; [g] [19.8, 23.0]; [h] [26.2, 27.5]; [i] [48.0, 54.0]; [j] [29.8, 30.0]; [k] [0.95, 1.00]; [l] [0.95, 1.00]; [m] [7.1, 7.8]; [n] [0.97, 1.15]; [o] [0.97, 1.15]; [p] [0.97, 1.15].

Δ	(kJ/mol)	[a]	−352	±	4
δ	(kJ/mol)	[b]	−24.8	±	0.2
$\nu^\circ_{>C=}$	(Å^3)	[c]	13.0	±	0.1
$\nu^\circ_{=O}$	(Å^3)	[d]	12.0	±	0.1
ν°_{-O-}	(Å^3)	[e]	16.0	±	0.2
ν°_{OH}	(Å^3)	[f]	16.0	±	0.2
ν°_{CH}	(Å^3)	[g]	20.9	±	0.2
$\nu^\circ_{CH_2}$	(Å^3)	[h]	26.5	±	0.3
$\nu^\circ_{CH_3}$	(Å^3)	[i]	50.0	±	0.5
$\nu^\circ_{H_2O}$	(Å^3)	[j]	30.0	±	0.3
β_{CH_2}		[k]	0.97	±	0.01
β_{CH_3}		[l]	1.00	±	0.01
α_{lip}	(10^{-4} K^{-1})	[m]	7.20	±	0.07
$\hat{d}_{wat,cyl}$		[n]	0.99	±	0.01
$\hat{d}_{wat,cap}$		[o]	1.01	±	0.01
$\hat{d}_{wat,pl}$		[p]	1.00	±	0.01

SAXS results for the micelles' size and shape agree well with those estimated by coarse-grained (MARTINI) Molecular Dynamics (MD) simulations [38]. Nevertheless, the SAXS measure for the thickness of the P80 hydrophilic shell, made of the very large three-branched molecule's headgroup, is larger, suggesting a higher degree of disorder than that estimated by MARTINI.

In particular, the number of bound molecules per polar head in the end-cap regions is large, ≈ 950 (Fig. 7H), corresponding, for the Eq. S73 of the SM, to a hydration level of ≈ 94% (Fig. 7J), in agreement with SANS experiments by Nayem et al. [51]. On the contrary, the number of bound water molecules in the cylindrical region per P80 and the hydration level are much lower, ≈ 110 and ≈ 66%, respectively (Fig. 7I and K).

We observe that the corresponding mass densities, $\hat{d}_{wat,cap}$ and $\hat{d}_{wat,cyl}$, of bound water embedded in the 1-domain of end-cap and cylinder regions are ≈ 1 (Table 2). Therefore, water near the end-cap areas, bound to polar heads, has a density similar to bulk water.

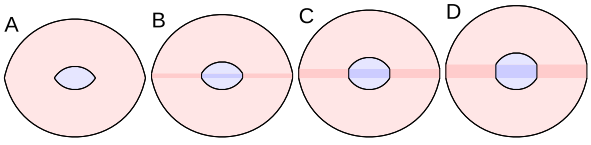

Fig. 8. Schematic representation of the P80-micelles shapes as from the ESRF-SAXS data analysis. The shapes A-D are for micelles formed by $m = 14$, 19, 24, and 29 self-assembled molecules, respectively. The inner azure regions represent the hydrophobic tails, while the pink regions represent the bulky hydrophilic side.

We report the trend of the area per polar head (Fig. 7L-O), that, as expected, displays differences among regions and interfaces within the same region. For example, the area between 1- and 2-domains in the end-cap region, ≈ 130 Å^2, almost doubles that in the cylinder region, ≈ 62 Å^2, (Fig. 7N and O).

Next, we calculate the concentration C_1 of free P80 molecules in solution as $C_1 = \alpha_1 C_{P80}$, where α_1 results from the numerical solution of Eq. (2) and C_{P80} is the total concentration of P80. In particular, we find that at the reference temperature $T_\circ$ (Fig. S13 of the SM) the P80 critical micellar concentration (cmc) is 0.014 ± 0.003 g/L, fully in agreement with literature [52].

3.3.2. Solid lipid nanoparticles

We find that the SAXS curves of our solid LNPs are fitted very well in the whole q range by the model described in Sect. 2.2.4, paragraph "SAXS of stacked polydisperse platelets in the form of barrel" (Fig. 6C-D). The values of the first-class fitting parameters for the chemical groups have a level of uncertainty $\ll 1$ Å^3 within reasonable validity ranges (Table 2). The mass density of bound water, relative to bulk, in contact with the P80 polar heads is $\hat{d}_{wat,pl} = 1.00 \pm 0.01$. The number of bound water molecules per P80 around the platelets is $r_{wat,P80} \simeq 100$ (Fig. 9A), much lower than the one found in P80 micelles, and the thickness of the polar head domain is very low, $t_1 \approx 5$ Å (Fig. 9E). Therefore, SAXS data show that the bulky P80 polar heads are well attached to the platelet surface. Indeed, the average distance between two adjacent P80

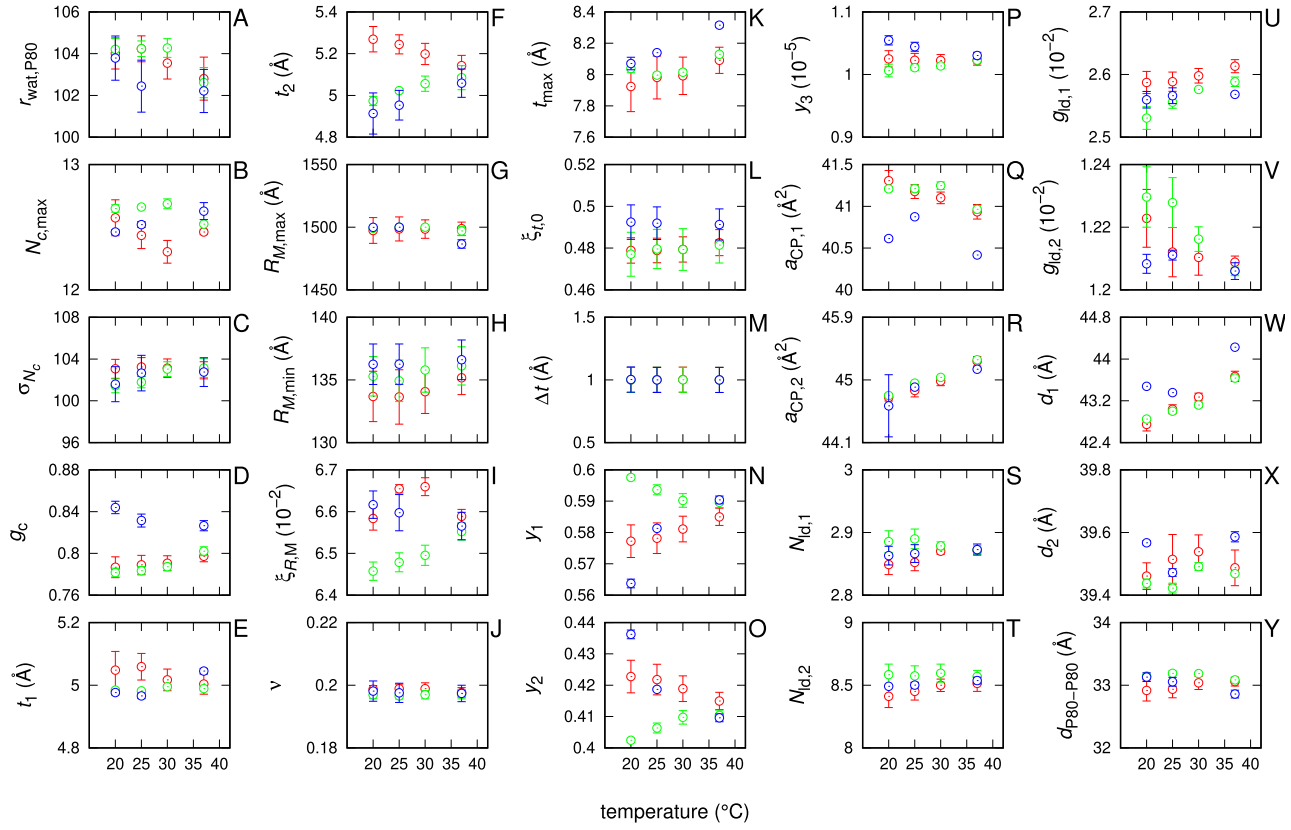

Fig. 9. Second-class fitting parameters (panels A, B, C, D, F, G, H, I, J, K, L, M, N, O, Q, R, S, T, U, V) and derived fitting parameters (panels E, P, W, X, Y) as from ESRF-SAXS data for LNPs (Fig. 6C-D). The parameters and symbols are defined in SM. Red, green and blue points refer to LNP concentration $C_{LNP} = 80.0$, 40.0, and 1.0 g/L, respectively. The validity ranges of the fit parameters shown in the panels are: A) [35,500]; B) [10,500]; C) [2,100]; D) [0,2]; F) [4,20] Å; G) [600,3000] Å; H) [100,400] Å; I) [0,5]; J) [0,1]; K) [3,40] Å; L) [0,10]; M) [0,30] Å; N) [0,1]; O) [0,1]; Q) [30,65] Å^2; R) [30,65] Å^2; S) [1,20]; T) [1,20]; U) [0,1]; V) [0,1].

molecules, Eq. S112 of the SM, is quite large, $d_{P80,P80} \simeq 30$ Å (Fig. 9Y) as necessary to get a narrow coating of P80 polar heads.

The fitting parameters allow us to evaluate that the average platelet surface associated with each P80 molecule, Eq. S113 of the SM, is 946 ± 6 Å^2, of which 325 ± 2 Å^2 is occupied by the P80 polar head and 622 ± 5 Å^2 by bound water. Furthermore, according to Eqs. S124-S126 of the SM, we find that the barrel is consisting of $66.1 \pm 0.1\%$ CP, $11.41 \pm 0.02\%$ P80 and $22.5 \pm 0.2\%$ bound water. In particular, we find that the small thickness of the layer between two platelets, is almost negligible ($\Delta t \approx 1$ Å, Fig. 9M). Considering that a water molecule's size is approximately 3 Å, this finding reveals that the thickness $\Delta t \approx 1$ Å must be considered as split between two stacked P80 layers. Therefore, the bound water molecules share this layer with P80 molecules and bridge their polar heads, as seen in phospholipid membranes [47,53]. Hence, two adjacent platelets collapse one on top of the other in a stacked conformation and comprise P80 polar heads, each hydrated by $\simeq 100$ bound water molecules. Without stacking, bound water within the P80 layer would form an interface with unbound water that would separate it from bulk water, as seen in phospholipid membranes [47]. When the platelets' surface is large enough instead, the system eliminates this interface, which would have a free energy cost, and reduces the total free energy by stacking the platelets into a barrel shape. Therefore, the platelets stacking is an enthalpy-driven process with an energy-favorable mechanism provided by the bound water. The fitting parameters allow us to evaluate the fraction of platelets' surface covered by P80 polar heads, Eq. S114 of the SM, as $\phi_{S,P80} = 0.343 \pm 0.002$, weakly dependent of temperature and solid LNP concentration. Therefore, $\approx 65\%$ of the platelet surface is covered by water bound to P80 and in contact with the layer of amorphous CP.

We estimate that the platelet has an inner radius, i.e. the radius of the maximum circular cross-section of the barrel, with a maximum value $R_{M,max} \approx 1500$ Å (Fig. 9G), with a polydispersion index of $\xi_{M,max} \approx 0.06$ (Fig. 9I), and minimum value $R_{M,min} \approx 130$ Å (Fig. 9H), with a bulging parameter $\nu \approx 0.2$ (Fig. 9J). Accordingly, the probability density, $p(R)$, of the platelet radius R assumes a peculiar shape (Fig. 10A), almost independent on temperature and solid LNP concentration.

The platelet core (made of CP) has a maximum half-thickness $t_{max} \approx 8$ Å (Fig. 9K), with a high level of polydispersion $\xi_{t,0} \approx 0.5$ (Fig. 9L). Moreover, the thickness of P80 hydrophobic chains, embedded in the platelet, is small $t_2 \approx 5$ Å (Fig. 9F). These values allow us to calculate the probability density of the whole platelet thickness, $2(t + t_1 + t_2)$. This density (Fig. 10D) is related to the probability density of the half-thickness core, $p_t(t)$, as $p(2(t + t_1 + t_2)) = (1/2)p_t(t)$.

The distribution of the number of platelets forming a barrel-like particle has a maximum at $N_{c,max} \approx 13$ (Fig. 9B), with a very large standard deviation $\sigma_{N_c} \approx 100$ (Fig. 9C) and distortion parameter, $g_c \approx 0.8$ (Fig. 9D). The CP amorphous domain occupies a negligible part of the platelets, $y_3 \approx 10^{-5}$ (Fig. 9P), whereas the CP 1-domain accounts for almost 58% of them, $y_1 \approx 0.58$ (Fig. 9N), with an area per molecule $a_{CP,1} \approx 41.5$ Å^2 (Fig. 9Q), a repeat distance $d_1 \approx 43$ Å (Fig. 9W), slightly increasing with temperature, and a repeat number $N_{ld,1} \approx 3$ (Fig. 9S). The CP 2-domain occupies only $\approx 42\%$ of each platelet, $y_2 \approx 0.42$ (Fig. 9O), with an area per molecule $a_{CP,2} \approx 45$ Å^2 (Fig. 9R) and a repeat distance $d_2 \approx 39.5$ Å (Fig. 9X), both increasing with temperature, and a repeat number $N_{ld,2} \approx 8$ (Fig. 9T).

Despite the low repeat numbers $N_{ld,1}$ and $N_{ld,2}$, the order degree of both lamellar domains 1 and 2 is high, with distortion parameters $g_{ld,1} \approx g_{ld,2} \approx 10^{-2}$ (Fig. 9U and V). The two lamellar orders agree with similar results found by Barbosa et al. [42], Lukowski et al. [54], and by Jenning and Gohla [55] for LNPs composed of cetyl palmitate.

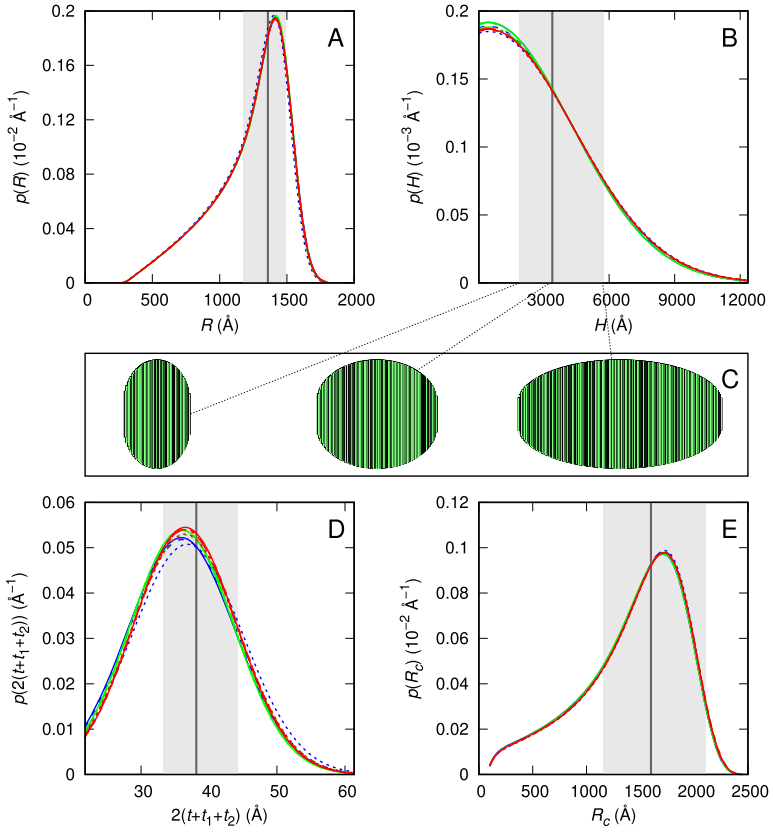

Fig. 10. Probability densities of the barrel circular cross-section radius R (panel A), the barrel height H (panel B), the total thickness of the platelets $2(t + t_1 + t_2)$ (panel D), and of the center-to-border distance R_c (panel E), as from ESRF-SAXS data for LNPs. Red, green, and blue lines refer to $C_{LNP} = 80.0$, 40.0, and 1.0 g/L. Solid, dotted, and dashed lines refer to temperatures 20, 25, and 37 °C. In all panels, the dark-gray vertical lines indicate the median at $C_{LNP} = 80.0$ g/L and 20 °C. The shaded areas mark the ranges between the 1st and the 3rd quartile in each distribution. Panel C represents three characteristic LNPs at 80.0 g/L and 20 °C, all with R_M, the maximum radius of the circular cross-section, corresponding to the 2nd quartile of $p(R_M)$ distribution ($R_M = 1520$ Å) and with total height H corresponding to the three quartiles of the $p(H)$ distribution (from left to right, 1860 Å, 3390 Å and 5740 Å) indicated by the three dotted-lines.

The fitting parameters also allow us to calculate the probability densities $p(H)$ and $p(R_c)$ of the whole barrel height H and the center-to-border distance R_c, respectively (Fig. 10B and E). We find that H has a broad distribution, with the median at 3390 Å, and the 1st and the 3rd quartile at 1860 Å and 5740 Å, respectively, corresponding to shapes (Fig. 10C) that resemble those observed by AFM (Fig. 5).

Nevertheless, it is essential to exercise caution when considering $p(H)$ because data on $H \geq 10^4$ Å are not directly accessible from the experimental q range. This information is derived from various constraints, such as concentrations and molecular volumes, and the approximations adopted in the model, e.g., the paracrystal theory.

The distribution $p(R_c)$ from our SAXS data is asymmetric and shifted toward large values, at variance with that derived from our AFM data (Fig. 5J) and the $p(R_H)$ from our DLS measurements (Fig. 4B). The median value is at $R_c = 1600$ Å, the 1st and the 3rd quartiles are at 1150 Å and 2100 Å, respectively. To comprehend the inconsistencies, it's essential to consider that the three methods have varying degrees of sensitivity regarding size. Specifically, SAXS measurements are obtained by averaging over a significant number of solid LNPs of the order of Avogadro's number, while AFM does not. As a result, SAXS data are considered to be more dependable than AFM. Therefore, we conclude that a representative shape for the LNPs (Fig. 11) corresponds to the medians of the distributions for H, R_M, and platelet thickness derived from SAXS data (Fig. 10).

From the SAXS measurements, we calculate, using Eq. S39 of the SM, the LNP's excess electron-density (ED) profile along the direction z (LNP's main axis) perpendicular to three subsequent platelets with split

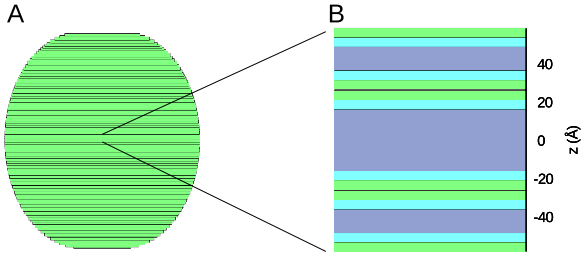

Fig. 11. Panel A: Representation of a LNP with external and internal dimensions corresponding to the medians of the distributions derived from the analysis of SAXS data at $C_{LNP} = 80.0$ g/L and 20 °C. (Fig. 10, $R_M = 1520$ Å, $H = 3390$ Å, $2(t_0 + t_1 + t_2 + \Delta t/2) = 39$ Å). Panel B: three platelets in the core, with layers schematically representing hydrated P80 polar heads (green), mixed P80 hydrophobic chains (cyan) embedded in amorphous CP (cyan) and lamellar CP (blue)). The thicknesses of the blue layers were sampled from the derived $p_t(t)$ distribution.

distance Δt (Fig. 12A). We set the half-thickness of the CP domain to its average value t_0, Eq. S31 of the SM. To note, the volume distribution functions of the hydrated P80 polar heads of a platelet, shown in green in Fig. 12B, are merged with that of the two adjacent platelets, indicating that the bound water acts as glue between the P80 polar heads belonging to two subsequent platelets. Sharp transitions in the profile between the P80 polar-head domain and the mixed P80 hydrophobic domain embedded in CP (shown in cyan) mark the thicknesses t_1 and t_2, respectively. Finally, a smoother transition indicates the interface between the latter and the CP domain (shown in blue).

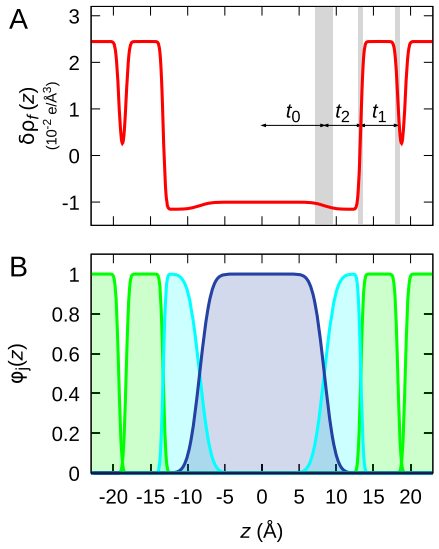

Fig. 12. Panel A: Excess ED profile of three subsequent platelets with split-thickness Δt within a LNP calculated from the global fit of the ESRF-SAXS data at $T = 20\,°C$ and $C_{LNP} = 80$ g/L (bottom curve in Fig. 6C-D). From right to left, the size of the shaded gray bands represents the standard deviation $\sigma_{pl,j}$, with the indexes $j = 1, 2, 3$ corresponding to outer, middle and inner domain, respectively, within the region $f = 3$ in Fig. 3B. Panel B: Volume fraction distributions $\phi_j(z)$, calculated according to Eq. S41-S43 of the SM, for the hydrated P80 polar head domain (green), the mixed P80 hydrophobic chain domain embedded in amorphous CP (cyan), and the crystalline CP domain (blue).

4. Conclusions

Through synchrotron light small-angle X-ray scattering measurements at varying temperatures and concentrations, we studied the solid LNPs formed by CP and stabilized by P80. To analyze our SAXS data, we created a novel structural model based on data gathered from dynamic light scattering (DLS) and atomic force microscopy (AFM) measurements. Our model effectively fits all SAXS curves in the full scattering vector range.

Based on our findings, the shape of our LNPs is polydisperse and barrel-like (Fig. 3A). This shape is achieved by stacking platelets (Fig. 3B). Each platelet contains a core with small crystalline domains of CP molecules. These molecules are elongated on the platelet surface and randomly rotated around the normal to the surface (Fig. 3C). The thickness of the CP core is also polydisperse, with an average thickness of around 8 Å.

Our study indicates that there are two different lamellar crystal structures in roughly equal proportions. These structures have characteristic (repetition) distances of approximately 43 and 39.5 Å, respectively, with repeat numbers of around 3 and 8 (Fig. 3D and E).

In contrast to the standard core-shell model, we discovered that the P80 molecules surround each platelet (Fig. 3B) and intercalate between them. Their polar heads are separated by an average distance of around 30 Å, occupying a layer of approximately 5 Å with roughly 100 water molecules bound to each head and bridging between them, with ≈ 1 Å between two stacked platelets. Instead, the P80 apolar tails are embedded within the amorphous CP portion, creating a layer roughly 5 Å thick.

According to our estimations, around 35% of the LNP's external surface and the surface of the internal platelets are hydrophilic, made up of P80 polar heads, with approximately 65% of bound water, which favors the platelets stacking. As a result, about 65% of the barrels' volume fraction is occupied by CP, 11% by P80, and the remaining is bound water.

We believe that these findings, based on our SAXS data and the new structural model for solid LNPs, are of paramount importance for creating effective devices to load and deliver therapeutics to their intended targets with improved accuracy and precision.

CRediT authorship contribution statement

Francesco Spinozzi: Writing – review & editing, Supervision, Software, Methodology, Investigation, Formal analysis, Conceptualization. **Paolo Moretti:** Writing – original draft, Investigation. **Diego Romano Perinelli:** Investigation. **Giacomo Corucci:** Investigation. **Paolo Piergiovanni:** Investigation. **Heinz Amenitsch:** Investigation. **Giulio Alfredo Sancini:** Conceptualization. **Giancarlo:** Writing – review & editing, Conceptualization. **Paolo Blasi:** Writing – review & editing, Supervision, Funding acquisition, Conceptualization.

Declaration of competing interest

The authors declare that they have no known competing financial interests or personal relationships that could have appeared to influence the work reported in this paper.

Data availability

Data will be made available on request.

Acknowledgements

The project work was funded by the "Ministero dell'Università e della Ricerca" PRIN 2017, project n. 20175XBSX4 (Targeting Hedgehog pathway: Virtual screening identification and sustainable synthesis of novel Smo and Gli inhibitors and their pharmacological drug delivery strategies for improved therapeutic effects in tumors) and partially funded by the European Union - Next Generation EU, Project Code: ECS00000041, Project Title: Innovation, digitalization and sustainability for the diffused economy in Central Italy - VITALITY. G.F. acknowledges the support by MCIN/AEI/ 10.13039/ 501100011033 and "ERDF A way of making Europe" grant number PID2021-124297NB-C31 and by the Ministry of Universities 2023-2024 Mobility Subprogram within the Talent and its Employability Promotion State Program (PEICTI 2021-2023). We acknowledge the European Synchrotron Radiation Facility (ESRF) for provision of synchrotron radiation facilities and we would like to thank Lewis Sharpnack for assistance and support in using beamline ID02. The authors thank ELETTRA for beam time allocation and support.

Appendix A. Supplementary material

Supplementary material related to this article can be found online at https://doi.org/10.1016/j.jcis.2024.02.076.

References

[1] R.H. Müller, K. Mäder, S. Gohla, Solid lipid nanoparticles (sln) for controlled drug delivery – a review of the state of the art, Eur. J. Pharm. Biopharm. 50 (1) (2000) 161–177.
[2] C. Tapeinos, M. Battaglini, G. Ciofani, Advances in the design of solid lipid nanoparticles and nanostructured lipid carriers for targeting brain diseases, J. Control. Release 264 (2017) 306–332.
[3] L. Xu, X. Wang, Y. Liu, G. Yang, R.J. Falconer, C.-X. Zhao, Lipid nanoparticles for drug delivery, Adv. NanoBiomed Res. 2 (2022) 2100109.
[4] R. Tenchov, R. Bird, A.E. Curtze, Q. Zhou, Lipid nanoparticles-from liposomes to mrna vaccine delivery, a landscape of research diversity and advancement, ACS Nano 15 (2021) 16982–17015.
[5] R. Dal Magro, B. Albertini, S. Beretta, R. Rigolio, E. Donzelli, A. Chiorazzi, M. Ricci, P. Blasi, G. Sancini, Artificial apolipoprotein corona enables nanoparticle brain targeting, Nanomed. Nanotechnol. Biol. Med. 14 (2018) 429–438.
[6] P. Blasi, A. Schoubben, G. Traina, G. Manfroni, L. Barberini, P.F. Alberti, C. Cirotto, M. Ricci, Lipid nanoparticles for brain targeting III. Long-term stability and in vivo toxicity, Int. J. Pharm. 454 (2013) 316–323.
[7] A. Akinc, M.A. Maier, M. Manoharan, K. Fitzgerald, M. Jayaraman, S. Barros, S. Ansell, X. Du, M.J. Hope, T.D. Madden, B.L. Mui, S.C. Semple, Y.K. Tam, M. Ciufolini, D. Witzigmann, J.A. Kulkarni, R. van der Meel, P.R. Cullis, The onpattro story and the clinical translation of nanomedicines containing nucleic acid-based drugs, Nat. Nanotechnol. 14 (2019) 1084–1087.

[8] X. Hou, T. Zaks, R. Langer, Y. Dong, Lipid nanoparticles for mrna delivery, Nat. Rev. Mater. 6 (2021) 1078–1094.
[9] G.P. Moss, P.A.S. Smith, D. Tavernier, Glossary of class names of organic compounds and reactivity intermediates based on structure (IUPAC recommendations 1995), Pure Appl. Chem. 67 (1995) 1307–1375.
[10] S. Doktorovova, E.B. Souto, A.M. Silva, Nanotoxicology applied to solid lipid nanoparticles and nanostructured lipid carriers – a systematic review of in vitro data, Eur. J. Pharm. Biopharm. 87 (2014) 1–18.
[11] M.J. Mitchell, M.M. Billingsley, R.M. Haley, M.E. Wechsler, N.A. Peppas, R. Langer, Engineering precision nanoparticles for drug delivery, Nat. Rev. Drug Discov. 20 (2021) 101–124.
[12] Y. Seo, H. Lim, H. Park, J. Yu, J. An, H.Y. Yoo, T. Lee, Recent progress of lipid nanoparticles-based lipophilic drug delivery: focus on surface modifications, Pharmaceutics 15 (2023).
[13] S. Haddadzadegan, F. Dorkoosh, A. Bernkop-Schnürch, Oral delivery of therapeutic peptides and proteins: technology landscape of lipid-based nanocarriers, Adv. Drug Deliv. Rev. 182 (2022) 114097.
[14] Lipid Nanoparticles Market, https://www.futuremarketinsights.com/reports/lipid-nanoparticles-market, 2023.
[15] V. Campani, S. Giarra, G. De Rosa, Lipid-based core-shell nanoparticles: evolution and potentialities in drug delivery, OpenNano 3 (2018) 5–17.
[16] D.L. Pink, O. Loruthai, R.M. Ziolek, P. Wasutrasawat, A.E. Terry, M.J. Lawrence, C.D. Lorenz, On the structure of solid lipid nanoparticles, Small 15 (2019) 1903156.
[17] D.L. Pink, O. Loruthai, R.M. Ziolek, A.E. Terry, D.J. Barlow, M.J. Lawrence, C.D. Lorenz, Interplay of lipid and surfactant: impact on nanoparticle structure, J. Colloid Interface Sci. 597 (2021) 278–288.
[18] H. Weyhers, S. Ehlers, H. Hahn, E. Souto, R. Müller, Solid lipid nanoparticles (sln)–effects of lipid composition on in vitro degradation and in vivo toxicity, Int. J. Pharm. Sci. Res. 61 (2006) 539–544.
[19] M.T. Jones, H.-C. Mahler, S. Yadav, D. Bindra, V. Corvari, R.M. Fesinmeyer, K. Gupta, A.M. Harmon, K.D. Hinds, A. Koulov, et al., Considerations for the use of polysorbates in biopharmaceuticals, Pharm. Res. 35 (2018) 1–8.
[20] P. Blasi, S. Giovagnoli, A. Schoubben, C. Puglia, F. Bonina, C. Rossi, M. Ricci, Lipid nanoparticles for brain targeting I. Formulation optimization, Int. J. Pharm. 419 (2011) 287–295.
[21] P. Blasi, A. Schoubben, G.V. Romano, S. Giovagnoli, A. Di Michele, M. Ricci, Lipid nanoparticles for brain targeting II. Technological characterization, Colloids Surf. B, Biointerfaces 110 (2013) 130–137.
[22] D. Nečas, P. Klapetek, Gwyddion: an open-source software for SPM data analysis, Cent. Eur. J. Phys. 10 (2012) 181–188.
[23] C.A. Schneider, W.S. Rasband, K.W. Eliceiri, Nih image to imagej: 25 years of image analysis, Nat. Methods 9 (2012) 671–675.
[24] T. Narayanan, M. Sztucki, P. Van Vaerenbergh, J. Léonardon, J. Gorini, L. Claustre, F. Sever, J. Morse, P. Boesecke, A multipurpose instrument for time-resolved ultra-small-angle and coherent X-ray scattering, J. Appl. Crystallogr. 51 (2018) 1511–1524.
[25] F. Spinozzi, C. Ferrero, M.G. Ortore, A.D.M. Antolinos, P. Mariani, GENFIT: software for the analysis of small-angle X-ray and neutron scattering data of macromolecules in-solution, J. Appl. Crystallogr. 47 (2014) 1132–1139.
[26] H. Kaya, Scattering from cylinders with globular end-caps, J. Appl. Crystallogr. 37 (2) (2004) 223–230.
[27] H.G. Thomas, A. Lomakin, D. Blankschtein, G.B. Benedek, Growth of mixed nonionic micelles, Langmuir 13 (1997) 209–218.
[28] J.P. Hansen, I.R. McDonald, Theory of Simple Liquids, Academic Press, London, 1976.
[29] M.S. Wertheim, Exact solution of the Percus-Yevick integral equation for hard spheres, Phys. Rev. Lett. 10 (1963) 321–323.
[30] F. Spinozzi, M.G. Ortore, G. Nava, F. Bomboi, F. Carducci, H. Amenitsch, T. Bellini, F. Sciortino, P. Mariani, Gelling without structuring: a SAXS study of the interactions among DNA nanostars, Langmuir 36 (2020) 10387–10396.
[31] M. Schmiele, T. Schindler, T. Unruh, S. Busch, H. Morhenn, M. Westermann, F. Steiniger, A. Radulescu, P. Lindner, R. Schweins, P. Boesecke, Structural characterization of the phospholipid stabilizer layer at the solid-liquid interface of dispersed triglyceride nanocrystals with small-angle X-ray and neutron scattering, Phys. Rev. E 87 (2013) 062316.
[32] M. Schmiele, C. Knittel, T. Unruh, S. Busch, H. Morhenn, P. Boesecke, S.S. Funari, R. Schweins, P. Lindner, M. Westermann, F. Steiniger, Analysis of the structure of nanocomposites of triglyceride platelets and DNA, Phys. Chem. Chem. Phys. 17 (2015) 17939–17956.
[33] R. Hosemann, S. Bagchi, Direct Analysis of Diffraction by Matter, North-Holland, Amsterdam, 1962.
[34] R. Hosemann, S.N. Bagchi, The interference theory of ideal paracrystals, Acta Crystallogr. 5 (1952) 612–614.
[35] R. Hosemann, K.L.W. Wilke, The paracrystal as a model for liquid crystals, Mol. Cryst. 2 (1967) 333–362.
[36] H. Matsuoka, H. Tanaka, T. Hashimoto, N. Ise, Elastic scattering from cubic lattice systems with paracrystalline distortion, Phys. Rev. B 36 (3) (1987) 1754–1765, https://doi.org/10.1103/PhysRevB.36.1754.
[37] D. Marsh, Molecular volumes of phospholipids and glycolipids in membranes, Chem. Phys. Lipids 163 (2010) 667–677.
[38] A. Amani, P. York, H. de Waard, J. Anwar, Molecular dynamics simulation of a polysorbate 80 micelle in water, Soft Matter 7 (2011) 2900–2908.
[39] M.G. Ortore, F. Spinozzi, P. Mariani, A. Paciaroni, L.R.S. Barbosa, H. Amenitsch, M. Steinhart, J. Ollivier, D. Russo, Combining structure and dynamics: non-denaturing high-pressure effect on lysozyme in solution, J. R. Soc. Interface 6 (2009) S619–S634.
[40] A. Piccinini, E. Lourenço, O. Ascenso, M. Ventura, H. Amenitsch, P. Moretti, P. Mariani, M. Ortore, F. Spinozzi, SAXS reveals the stabilization effects of modified sugars on model proteins, Life 12 (2022).
[41] A. Gordillo-Galeano, C.E. Mora-Huertas, Solid lipid nanoparticles and nanostructured lipid carriers: a review emphasizing on particle structure and drug release, Eur. J. Pharm. Biopharm. 133 (2018) 285–308.
[42] R.M. Barbosa, B.R. Casadei, E.L. Duarte, P. Severino, L.R.S. Barbosa, N. Duran, E. de Paula, Electron paramagnetic resonance and small-angle X-ray scattering characterization of solid lipid nanoparticles and nanostructured lipid carriers for dibucaine encapsulation, Langmuir 34 (2018) 13296–13304.
[43] P. Blasi, S. Giovagnoli, A. Schoubben, M. Ricci, C. Rossi, Solid lipid nanoparticles for targeted brain drug delivery, Adv. Drug Deliv. Rev. 59 (2007) 454–477.
[44] A.L.R. de Souza, T. Andreani, F.M. Nunes, D.L. Cassimiro, A.E. de Almeida, C.A. Ribeiro, V.H.V. Sarmento, M.P.D. Gremião, A.M. Silva, E.B. Souto, Loading of praziquantel in the crystal lattice of solid lipid nanoparticles, J. Therm. Anal. Calorim. 108 (2012) 353–360.
[45] L.A. Feigin, D.I. Svergun, Structure Analysis by Small-Angle X-Ray, Neutron Scattering, Plenum Press, New York, 1987.
[46] O. Glatter, O. Kratky, Small Angle X-Ray Scattering, Academic Press, New Press, 1982.
[47] C. Calero, G. Franzese, Membranes with different hydration levels: the interface between bound and unbound hydration water, J. Mol. Liq. 273 (2019) 488–496.
[48] F. Spinozzi, L. Paccamiccio, P. Mariani, L.Q. Amaral, Melting regime of the anionic phospholipid dmpg: new lamellar phase and porous bilayer model, Langmuir 26 (2010) 6484–6493.
[49] T. Frühwirth, G. Fritz, N. Freiberger, O. Glatter, Structure and order in lamellar phases determined by small-angle scattering, J. Appl. Crystallogr. 37 (2004) 703–710.
[50] P. Moretti, P. Mariani, M.G. Ortore, N. Plotegher, L. Bubacco, M. Beltramini, F. Spinozzi, Comprehensive structural and thermodynamic analysis of prefibrillar WT α-synuclein and its G51D, E46K, and A53T mutants by a combination of small-angle X-ray scattering and variational Bayesian weighting, J. Chem. Inf. Model. 60 (2020) 5265–5281.
[51] J. Nayem, Z. Zhang, A. Tomlinson, I.E. Zarraga, N.J. Wagner, Y. Liu, Micellar morphology of polysorbate 20 and 80 and their ester fractions in solution via small-angle neutron scattering, J. Pharm. Sci. 109 (2020) 1498–1508.
[52] Y. Bide, M.A. Fashapoyeh, S. Shokrollahzadeh, Structural investigation and application of tween 80-choline chloride self-assemblies as osmotic agent for water desalination, Sci. Rep. 11 (2021) 17068.
[53] F. Martelli, C. Calero, G. Franzese, Redefining the concept of hydration water near soft interfaces, Biointerphases 16 (2021) 020801.
[54] G. Lukowski, J. Kasbohm, P. Pflegel, A. Illing, H. Wulff, Crystallographic investigation of cetylpalmitate solid lipid nanoparticles, Int. J. Pharm. 196 (2000) 201–205.
[55] S.H.G. Volkhard Jenning, Encapsulation of retinoids in solid lipid nanoparticles (sln), J. Microencapsul. 18 (2001) 149–158.